STUDY OF DRAG REDUCTION IN MICROSTRUCTURED CHANNEL WITH

PATTEREND CAVITIES AND WETTABILITY CONTROL

_____

A Thesis

presented to

the Faculty of the Graduate School

at the University of Missouri-Columbia

_____

In Partial Fulfillment

of the Requirements for the Degree

Master of Science

_____

by

Jingwen Hu

Dr. C.L. Chen, Thesis Supervisor

December 2016

The undersigned, appointed by the dean of the Graduate School, have examined the thesis entitled

STUDY OF DRAG REDUCTION IN MICROSTRUCTURED CHANNEL WITH

PATTEREND CAVITIES AND WETTABILITY CONTROL

Presented by Jingwen Hu

A candidate for the degree of Master of Science

And hereby certify that in their opinion it is worthy of acceptance.

_____

Professor C.L. Chen

_____

Professor Gary Solbrekken

_____

Professor Stephen Montgomery-Smith

ACKNOWLEDGEMENTS

First and foremost, I would like to express my sincere gratitude to Dr. Chen for the valuable guidance and advice. He inspired me greatly to work in my research. His willingness to motivate me contributed tremendously to my research project.

I would also like to thank Dr. Gary Solbrekken and Dr. Stephen Montgomery-Smith for their willingness to be members of my thesis committee and for offering me with kind help to complete this research program.

In addition, I would like to thank my lab mate, Sean and Zhaoqing, for their help and encouragement, especially Sean and Zhaoqing, who gave me lots of helpful suggestions. Finally, an honorable mention goes to my parents and friends for their supports and help on us in completing this research program.

TABLE OF CONTENTS

LIST OF ILLUSTRATIONS

LIST OF TABLES

ABSTRACT

This work is done in part as a requirement towards the fulfillment of the master's degree. Four chapters are covered in this work.

Chapter 1 gives an overview of the various works that have been done in the field, including some basic background and theory.

Chapter 2 discusses the details of the numerical model. Grid independency study and validation of these models are accomplished by comparing with the analytical solution and quantitatively with the experiments.

Chapter 3 explores the parametric study of different initial condition and geometries. Here, we are particularly interested in the effects of initial interface assumption. It is found that the effective slip length of preset interface assumption is in good agreement with the initially air-filled interface assumption, as well as the experimental results, at low gas fraction. However, the effective slip length of a preset interface has a dramatic deviation at high gas fraction with the initially air-filled channel. Large difference occurs when changing the surfaces from hydrophobic to hydrophilic. For a preset interface, air patterns are trapped in the structured cavities and compressed by the liquid flow. An air-water interface still exists even the surface of the cavity is hydrophilic, thus, drag reduction increases. However, for an initially air-filled microchannel, water expel the air out of the microchannel and completely wets the whole channel at the end. No air-water interface is found and drag reduction decreases. Studies also show that drag reduction increases when increasing the contact angle of the cavity surfaces. To extend our work further, parametric studies have been carried out to investigate the effect of geometry by changing the cavity width, fraction and numbers at low gas fraction. It is found that increasing the gas fraction and decreasing

the cavity numbers can provide better performance on drag reduction, as the interfaces provide longer and continuous slip-boundary condition.

Conclusions and future works are discussed in Chapter 4. More cases are carried out to build the relationship between friction reduction and different configurations in transient state to find a smaller range of depth-to-width ratio in which the air pockets can be successfully trapped in the cavity. Different shapes of posts can be studied to observe the position of the air-water interface because the mechanism for depinning is strongly dependent on the details of the post geometry and on the Young's contact angle, and depinning from both the top and the side edges of the posts is important in controlling the fluid behavior. The effect of air diffusion and how to overcome this effect will be taken into consideration.

Chapter 1. INTRODUCTION

In this chapter, the motivation and background for this research is discussed as well as the structure of this thesis. Some basic principles of drag reduction are explained and the definition of several important parameters is described.

1.1 Motivation

Microchannel is widely used in microfluidic devices, micro-electro-mechanical-systems (MEMS) and lab-on-a-chip systems. However, the reduced size of channel results in higher surface-to-volume ratio and higher frictional loss[1]. Therefore, the pumping power for the transportation of liquid through microchannel is relatively large. The skin-friction reduction in microchannel flows can help minimize the pressure loss in pipe flow and alleviate the pumping power requirements.

Currently, state of art methods for significantly reducing drag have been extensively investigated by many researchers [2-16]. Active methods, such as injection air bubbles by Sanders et al. [2] and surface blowing and suction control by Kim et al. [3], were considered. Passive methods, such as optimizing surface micro-texturing geometry by Han et al. [4], and addition of polymers by Hong et al. [5], were considered. However, for the evaluation of the economics, the active methods are not considered as an efficient method because they require an additional energy input.

One approach proposed for reducing the skin friction of liquid flow in microchannel is patterning cavities with superhydrophobic coating, and was relatively investigated through theoretical [6,7], experimental [8-13], and numerical studies [8-9,13-16]. Air layer can be sustained passively with small energy consumption and the

contact area between the solid wall and the liquid flow is minimized, resulting in a reduction of drag.

Philip [6] was the first to theoretically study the flow in a channel with longitudinal and transverse ridges, assuming that the flow is Stokes flow and the gas-liquid interface is flat. Lauga & Stone [7] extended their work to a circular tube with alternate shear-free slots oriented both transverse and longitudinal to the direction of the flow and obtained analytical relations for the effective slip length with mixed boundary conditions. They predicted that for a given flow geometry, the drag reduction was only a function of fraction and shear-free area and the dimensionless channel depth, whereas the slip length was independent of channel height. Their formula for the estimation of slip length in a given geometry agreed well with Lee et al. [11] and Park et al. [17].

Qu and Rothstein et al. [8,9] were among the first to demonstrate experimentally that microstructured channel with superhydrophobic surfaces can produce drag reduction and an apparent slip in laminar flows. More recent experiments such as Choi et al. [10], Lee et al. [11] Tsai et al. [12] extended their works to a wide range of geometries.

Numerical simulations provided additional information about the effects of hydrophobic surfaces. Maynes et al. [13] investigated the drag reduction performance in microchannel with ridges aligned longitudinal and transverse to the flow direction. Their results showed that the effective slip length and friction reduction increase with increasing relative cavity width, cavity depth and decreasing cavity length. Cheng et al. [14] also studied the effect of effective slip length numerically for various surface patterns as a function of gas fraction. Wang et al. [15] extended this work further to longitudinal shear-free slots in a circular tube. However, in all the models, the shape of the liquid-gas interface was idealized as flat at initial condition. Davies et al. [16]

previously made a comparison between their experimental and numerical results using continuum CFD methods for the flow through microchannels with superhydrophobic surfaces patterned with transverse grooves on both sides. It was reported that their experimental results for the effective slip length agreed well with their computational results at low gas fractions. For higher gas fraction, their experiment results were approximately 50% less than their numerical results. Similar trends were observed by other researchers [13-14, 17]. In the experimental work of Tsai et al. [12], they found that the air-water meniscus curvature played an important role in microflows over hydrophobic microridges and might be the reason for the difference between experiments and numerical simulations. Gaddam et al. [18] employed an unsteady volume of fluid model to investigate the behavior of the liquid-gas meniscus. They found that the difference between the experimental and previous numerical results was attributed to channel end-wall effects as well as the flat interface assumption. However, in their simulations, the gas phase was assumed to be incompressible and the surface wettability of the substrate was not considered.

Since the behavior of the initial gas-liquid interface has a pronounced effect on the effective slip length and thus on flow resistance, the idealization of a flat air-water interface no longer serves as an effective boundary condition at higher gas fraction. In addition, the initial condition and starting-up process can be critical to the final state of interface. In the present work, a volume of fluid (VOF) model has been used for interface capturing at the liquid-gas meniscus, thereby predicting the physics of the flow. In the first part of the work, a transient air trapping process is simulated in a single micro-structured cavity with two interface conditions at different contact angle. One is the preset flat interface assumption and the other is the initially air-filled microchannel assumption. In the second part of the research, we extend our work further to simulate

multiple cavities at low gas fraction, to investigate the efficiency of these geometries in reducing pressure drop across micro-channels in a laminar regime.

1.2   Background

1.2.1 Superhydrophobic surface

Water will bead on the surface of lotus leaves and roll around as droplets. These leaves exhibit considerable superhydrophobicity (Figure 1.1). This phenomenon is known as the lotus effect. Loose dirt particles will be gathered up by the water droplets as they roll, leaving a clean and dry surface.

Figure 1.1: Water droplet bead on lotus leaf

It has been reported that nearly all superhydrophobic and self-cleaning leaves consist of an intrinsic hierarchical structure (Figure 1.2) [19]. The study of superhydrophbic surfaces have been inspired by this phenomenon, with two major models called Cassie-Baxter and Wenzel to describe the behavior of liquid droplet on rough surface [20,21]. This section of the literature review considers the fundamentals of surface tension, wetting and capillarity, and how these can explain the observed properties of superhydrophobic surfaces.
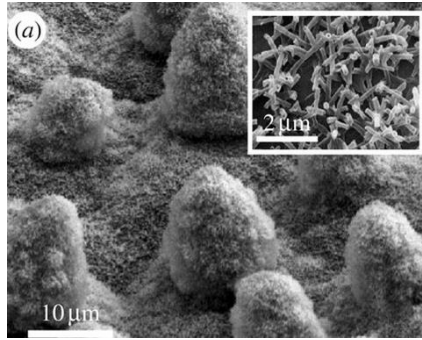
Figure 1.2: SEM micrographs of hierarchical structures in lotus leaf

Surface tension is a force that operates on a surface and acts perpendicularly and inwardly from the boundaries of the surface, which tends to decrease the area of the interface. As a result, a liquid will form a shape having minimum area.

Since the major phenomenon of the Cassie-Baxter state, where pockets of air exist between the microtexture cavities, the three phase interface characteristics are an important parameter. If a liquid is dispensed on a solid substrate, the liquid either completely wet or partially wet the solid substrate. This depends on the spreading parameter,

$$S = \gamma_{SG} - (\gamma_{SL} + \gamma)$$

Where γ_{SG} is the solid-vapor surface energy, γ_{SL} is the solid-liquid energy and γ is the liquid-vapor surface energy, or what is commonly referred as surface tension. When S>0, the surface will try to lower its energy by spreading the dispensed liquid until it is completely wetted, and if S<0, the liquid will try to minimize its footprint by forming a compact droplet or dome on the substrate, partial wetting occurs.

S>0 (completely wet)   S<0 (partially wet)
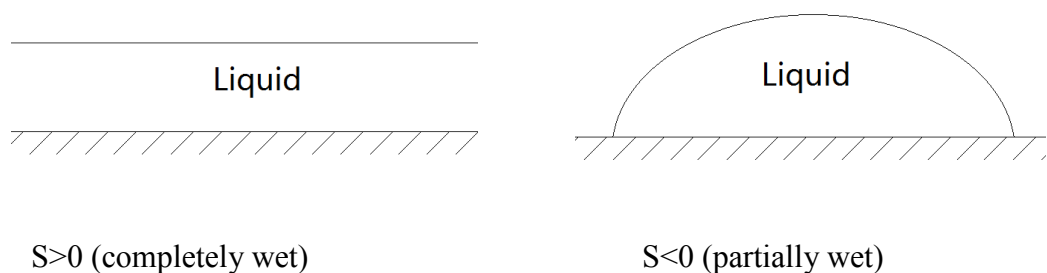
Figure 1.3: Schematic representation of the spreading parameter.

Combining the spreading parameter definition with the Young relation yields the Young-Dupre equation:

$$S = \gamma_{LG}(cos\theta - 1)$$

Which only has physical solution for θ when S < 0.

Young's Equation can be interpreted as forces being exerted on the three phase contact line (black circle in figure) which are parallel to the surface must sum to zero if the system is at equilibrium. Young's equation [22] gives the relation between the equilibrium contact angle θ and the three surface tensions as

$$\gamma_{SG} = \gamma_{SL} + \gamma_{LG}cos\theta$$

Where subscript SG refers to solid-gas, SL to solid-liquid, LG to liquid-gas and θ to the contact angle. The contact angle can be used to describe the wettability of the liquid. When a water drop on a surface has a contact angle less than 90 degree, the surface becomes wetting and is called a hydrophilic surface which has an affinity for water. When the contact angle is larger than 90 degree, the surface is called a hydrophobic surface which tends to repel water. These equations are based on the equilibrium state. Therefore, the contact angle defined by Eq. is sometimes known as the equilibrium contact angle.
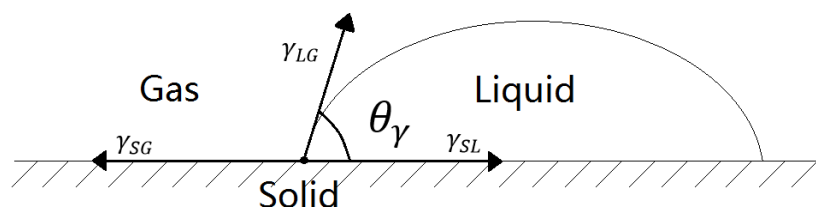
Figure 1.4: Schematic representation of Young's contact angle

Surface tension leads to a pressure difference generated between the inside and outside of a curved interface and is known as the Laplace pressure,

$$\Delta p = \gamma(\frac{1}{r_1} + \frac{1}{r_2})$$

Where r_1 and r_2 are the radii of curvature of the interface. Bubbles and drops are often spherical, where r_1 and r_2 are equal so that the equation can be simplified to,

$$\Delta p = \frac{2\gamma}{r}$$

The Young's equation holds for flat surfaces, however, when the surface is roughened or textured, the situation changes. Two wetting states can be envisaged when a drop is deposited on to a heavily roughened surface. In one the liquid could penetrate the features completely wetting the surface, in another the water could sit on top of them with a gas layer underneath; these two situations were approached by Wenzel in 1936 and Cassie –Baxter in 1944, respectively [20,21]

Wenzel State   **Cassie-Baxter State**
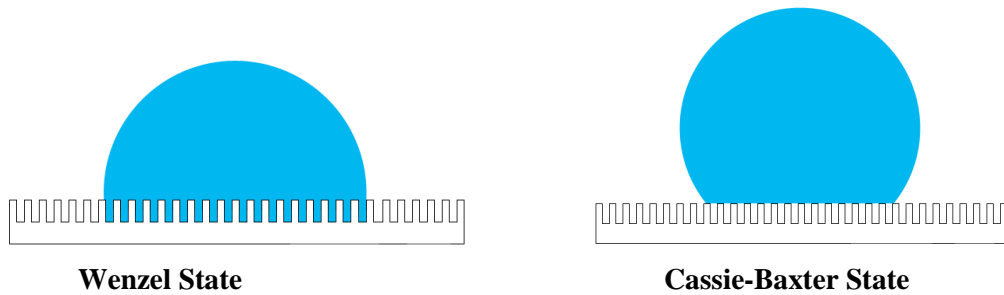
Figure 1.5: A drop of water on a surface with posts. The drop in the Wenzel state penetrates the space between the posts and wets the bottom of the surface. In the Cassie-Baxter state the drop sits on top of the posts with cushion of air beneath it.

The Wenzel state represents a liquid droplet that is completely in contact with the microstructured surface. The apparent contact angle θ_w is described by the following equation

$$\cos\theta_w = r\cos\theta_Y$$

where r is the ratio of the actual area to the projected area and θ_Y is the equilibrium Young's contact angle on the smooth surface.

This equation predicts that the degree of roughness will amplify the wetting character of the surface. Hydrophilic surfaces will become more hydrophilic and

hydrophobic more hydrophobic. Experiments show that flow past through a surface of Wenzel State will increase the drag.

On the other hand, the Cassie-Baxter state characterizes a liquid droplet that is suspended on tops of microstructures without penetrating the cavities. The apparent contact angle of Cassie-Baxter state θ_{CB} is expressed by the following equation

$$\cos\theta_{CB} = \emptyset_s(cos\theta_Y + 1) - 1$$

where $\emptyset_s$ is the solid fraction ratio between the actual wetted area of the solid and the nominal area. θ_Y is the Young's contact angle, and θ_{CB} is the Cassie-Baxter angle.

To ensure the Cassie-Baxter state, the surface topography must be rougher than the critical roughness factor

$$r_c = \emptyset_s - \frac{1 - \emptyset_s}{cos\theta_Y}$$

Where r_c is the critical roughness factor. A roughness factor lower than r_c will result in a Wenzel state. On the other hand, a roughness factor higher than r_c will lead to a stable Cassie state.

In the Cassie-Baxter state, the hierarchical surfaces trap the air bubbles within the structures, which can provide slippery air-water interfaces.

Studies have shown that the presence of these air pockets in the Cassie-Baxter state can lead to drag reduction. [3-12]

Figure 1.6 shows a model of the superhydrophobic surface in Cassie-Baxter state. The surface is microtextured with regular ridges. Instead of wetting the entire surface, the water bead only on the top of the microridges and resulting in the air-water interface. This model was verified in Ou's paper and is employed to explain the reason for observed drag reduction in laminar flows. It is common understanding that flow past

through a surface of Cassie-Baxter state will reduce drag and has been extensively studied.
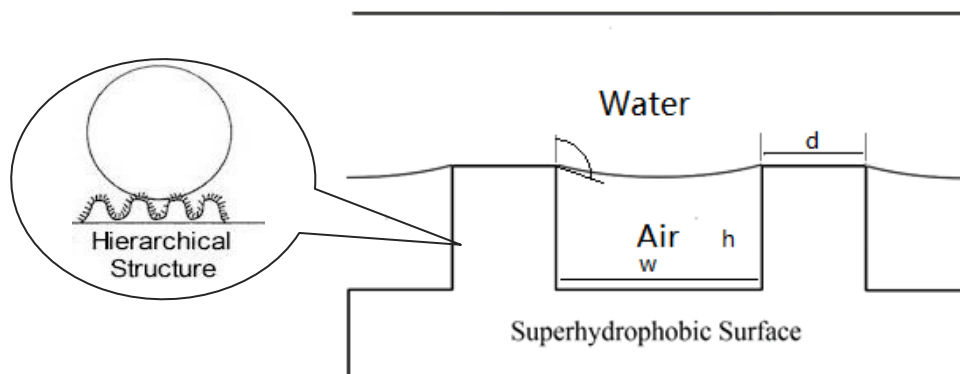
Figure 1.6: Model of Superhydrophobic Surface with Microstructured Ridges under Cassie-Baxter State

On a real surface there is always a range in which the contact angle fails, the upper and lower bounds can be found by advancing and receding the three phase contact line over the surface. The contact angle hysteresis is the difference between these two values, and determines the degree of mobility a drop will have on the surface. Contact angle hysteresis is caused by chemical and structural heterogeneity causing pinning of the three phase contact line.

Typically superhydrophobic surfaces have a very small contact angle hysteresis, which leads to a very small force being required to initiate drop movement. A tiny tilt to the substrate will allow the drop to roll off, picking up any debris on the surface and taking it with it, this is known as the self-cleaning or the lotus effect.

1.2.2 Slip on superhydrophobic surfaces: Laminar flows

It is widely accepted that in fluid dynamics, the boundary condition for a viscous fluid at a solid wall is no-slip condition. The fluid velocity at all fluid-solid boundaries is equal to that of the solid boundary.

Figure 1.7 illustrates a schematic of slip velocity and slip length of laminar flow through infinite parallel plates. If the interface is between fluid and solid, the value of the slip length (b) is relatively small, then the no-slip condition exists, where zero velocity can be assumed at the solid surface. If the interface is between fluid and gas, the value of the slip velocity (u_{slip}) and slip length (b) are no longer small. Though the fluid does experience some drag at the interface, it is relatively small compared to the drag exerted on the solid wall, thus, the interface can still be assumed to be free-shear.
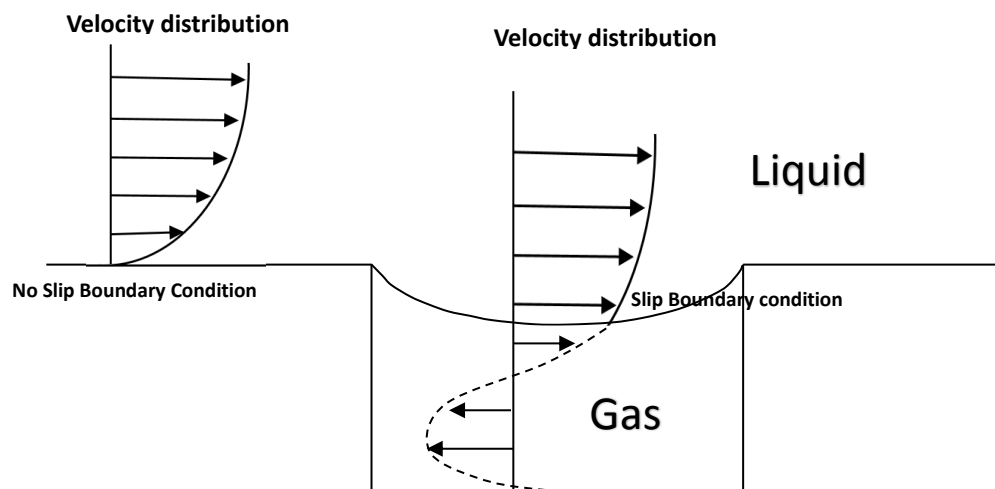
Figure 1.7: Demonstration of the mechanism of the micro-grooved surface

Most works on drag reduction with superhydrophobic surfaces has involved flow in the laminar regime. Philip [6] was the first to analytically study on the Stokes shear flows past superhydrophobic surfaces with arrays of transverse or longitudinal shear-free slots, and more recently Lauga & Stone and Cottin-Bizonne et al. [7] analytically solved the Stokes flow problem of flow past surfaces or through channels with mixed boundary conditions (one wall is no-slip whereas the other wall contains a shear-free boundary condition). Numerical simulations for this matter typically assumed that the boundary condition between the solid and liquid is no-slip; the liquid-vapor interface is assumed to be flat and shear-free so that the viscosity (flow resistance) or the air trapped within the surface is negligible.

(1) Effective Contact Area

Since the surface are superhydrophobic, the liquid will not penetrate the cavity but will form a meniscus interface between the peaks. Consequently, a significant reduction in the contact surface area can be achieved.

Considering a static analysis of the problem, Young's Law can be implemented to determine the pressure loss,

$$\Delta P = p_w - p_a = \frac{4\gamma}{w \; \cos(\pi - \theta)} \qquad (1.1)$$

where the w refers to water and a refers to air. γ is the surface tension of the fluid in question and θ is the contact angle. If the contact angle falls below 90° or w is increased beyond a certain limit, no interface will be supported. Thus, with proper contact angle, spacing and pressures, the fluid rests on tops of the microridges and has large areas of free surface between them. Previous works show that for large post spacing, drag is decreasing due to less effective surface area and increasing drag over the tops of the microridges.

(2) Slip velocity and slip length

Slip velocity and slip length at the surface are usually used as a measure of drag reduction in microchannels. The fully-developed, incompressible flow of a constant property Newtonian fluid between parallel planes is considered in the following analysis. Two parallel planes of infinite extent in the x- and z- directions are separated by a distance H in the y- direction.

For fully-developed laminar flow, the momentum and mass conservation equations reduce to the following equation,

$$\frac{\partial^2 u}{\partial y^2} = \frac{1}{\mu} \left(\frac{dp}{dx}\right)$$ (1.2)

Where u is the fluid velocity in the x- direction, dp/dx is the pressure gradient in the x- direction and μ is the viscosity of the fluid.

Navier had first proposed a slip boundary condition and is show schematically in Fig. In Navier's model, the slip velocity is proportional to the shear stress.

$$u_{\text{wall}} = b \frac{\partial u_{slip}}{\partial y}$$ (1.3)

here b is the slip length, u_{slip} is the average velocity at the superhydrophobic surface and $\frac{\partial u_{slip}}{\partial y}$ is the shear rate at the wall.
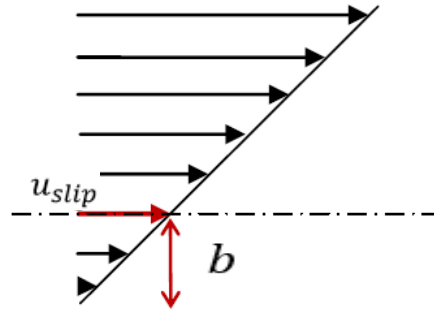
Figure 1.8: Scheme of slip velocity at the wall

If one considers the case where only the lower channel wall exhibits slip, the following boundary conditions are applicable:

$$u = 0 \; at \; y = 0,$$ (1.4)

$$u = -b \frac{\partial u}{\partial y} \; at \; y = H.$$ (1.5)

Note that, for convenience, the lower wall of the microchannel has been chosen as the slip wall and, as such, the slope of the velocity gradient is negative. The solution of Eq.1.3 with boundary condition 1.4 and 1.5 results in the following velocity profile:

$$u(y) = \left(\frac{dp}{dx}\right)\left(\frac{1}{2\mu}\right)\left(y\left(\frac{H^2+2bH}{H+b}\right) - y^2\right)$$ (1.6)

The mean velocity, volumetric flow rate per unit width and friction factor follow from eq., respectively, as:

$$u_m = \left(\frac{dp}{dx}\right)\left(\frac{H^2}{12\mu}\right)\left(\frac{H+4b}{H+b}\right) \tag{1.7}$$

$$q = \left(\frac{dp}{dx}\right)\left(\frac{H^3}{12\mu}\right)\left(\frac{H+4b}{H+b}\right) \tag{1.8}$$

and

$$f = \frac{96\left(\frac{1+b/H}{1+4b/H}\right)}{Re} \tag{1.9}$$

Two different boundary conditions are implemented in the numerical simulations. First, the solid-liquid interface at the wall is taken to be no-slip, which means that all of the velocity at the wall surface is zero. Second, the liquid-gas interface between the microridges is treated as shear-free, which means viscosity is vanished.

(3) Parameter – fRe, λ_T and Reduction(%)

In these simulations, the pressure drop is evaluated and converted into f·Re. In an incompressible, laminar flow for a channel with smooth walls, the factor is expressed as

$$fRe = \frac{2\Delta P \cdot A D_h^2}{\mu Q L} \tag{1.10}$$

where the Reynolds number is based on the hydraulic diameter, D_h

$$D_h = 2H \tag{1.11}$$

$$Re = \rho u_i D_h/\mu \tag{1.12}$$

The hydraulic diameter is defined as four times the cross sectional area, A. f is called the friction factor, which represents the integrated frictional resistance. ΔP is the pressure drop from the inlet to the outlet. μ is the absolute viscosity of the liquid, and L is the cavity length. fRe serves as a valuable metric for comparing drag reduction.

For a classical Poiseuille flow through a smooth channel, the Poiseuille number is given by $f \cdot Re = 96$. However, in our study, the flow is not fully developed and the velocity profile is quite different due to the entrance effect. Hence, a clean microchannel with pressure inlet has been studied. The standard Poiseuille number in present work is calculated as $f \cdot Re = 90.27$ and will be evaluated in the following sections.

Numerical predictions show that the reduction in the classical friction factor-Reynolds number product increase with increasing relative cavity width, increasing relative cavity depth, and decreasing relative microrib/cavity module length.

The normalized effective slip length is a function of product of the Darcy friction factor and Reynolds number f·Re for channel flow and expressed is as Maynes et al 2007,

$$\frac{\lambda_T}{H/2} = \frac{32}{f \cdot Re} - \frac{1}{3} \tag{1.13}$$

This expression is used to compare the present numerical predictions with experimental results of Qu et al [9].

The reduction in pressure drop is given by

$$\text{reduction in pressure drop}(\%) = \frac{\Delta P_{Smooth} - \Delta P_{Textured}}{\Delta P_{Smooth}} \times 100 \tag{1.14}$$

where ΔP_{Smooth} and $\Delta P_{Textured}$ correspond to the pressure drop in smooth and textured channels, respectively.

1.2 Objectives

This work is to present a numerical simulation with a two-phase VOF model. In the first part of the work, a transient air trapping process is simulated in a single micro-structured cavity with different surface wettability and interface conditions. Two parallel cases are studied in the same microchannel with different initial interface conditions. One is with an initially air-filled microchannel and water flows from the inlet. The other is with a preset flat interface initially at the cavity. In the second part of the research, we extend our work further to simulate multiple cavities at low gas fraction, to investigate the efficiency of these geometries in reducing pressure drop across micro-channels in a laminar regime. The results are compared with those of the simplified model to estimate the deviation due to the assumptions. The results of our work extend our understanding on the friction reduction by wettability control and provide a reference to the manifold/micro-channel designer.

Chapter 2. Methodology

This research is conducted using the commercial software of ANSYS FLUENT 14.5, which is a powerful computational fluid dynamics (CFD) tool for simulating fluid flows. CFD modeling contains geometry creation, grid generation and computation, which are discussed in the following sections.

2.1 Governing Equation

Commercial software, ANSYS FLUENT 14.5, was used to analyze the fluid flow through the microstructured channel. In this simulation, a volume of fluid (VOF) in Fluent is employed to track the interface between water and gas in addition to the continuity and momentum equations.

The Navier-Stokes and continuity equations, as provided here:

$$\nabla \cdot V = 0 \tag{2.1}$$

$$(V \cdot \nabla)V = -\frac{1}{\rho}\nabla p + v\nabla^2 V \tag{2.2}$$

where equation 2.1 is called the continuity equation for constant density and equation 2.2 is the Navier-Stokes equations for incompressible constant viscosity flow. These equations can be used to solve incompressible flow.

The Volume of Fluid (VOF) model in two-dimensional form was used to solve the equation for volume fraction in addition to conserving mass and momentum. The VOF method is based on the concept of a fluid volume fraction. Within each control volume, it is customary to retain only one value for each flow quantity. It is easier to locate surfaces and determine surface curvatures if the amount of fluid in each cell is known because the surfaces lie in cells partially filled with fluid or between cells full of fluid

and cells that have no fluid. Curvatures are computed by using the fluid volume fractions in neighboring cells.

FLUENT uses the Finite Volume Method (FVM) for discretization of the governing equations in order to convert them to algebraic equations which are solved numerically. This technique uses control volumes which are defined by grid elements. The discrete values for the flow variables are stored in the cell centers by Fluent, however for the computation of the convective terms the cell face values are required and these are interpolated from the cell center values using an upwind scheme. More details on the computation algorithm and the Finite Volume Method can be found in the Fluent manual [33].

2.2   Model Setup

In this research, several simulations with different types of geometry are performed. The effects of various texture geometries on pressure drop reduction across the channel have been investigated. The computational domain illustrated schematically in figure 2.1 is considered. The length (L) of the domain for all geometries is 20 μm and the height of the microchannel (H) is 6 μm. The length of the ridge varies from 1 to 6 μm and the maximum height of ridge (h) in all cases has been maintained as 2 μm. The spacing between adjacent ridges is varied due to different gas fraction. The input velocities chosen for the simulation are in the range of 0.1 to 5 m/s corresponding to $10 < \text{Re} < 50$. The parameters pertaining to the simulations are presented in table 2.1.
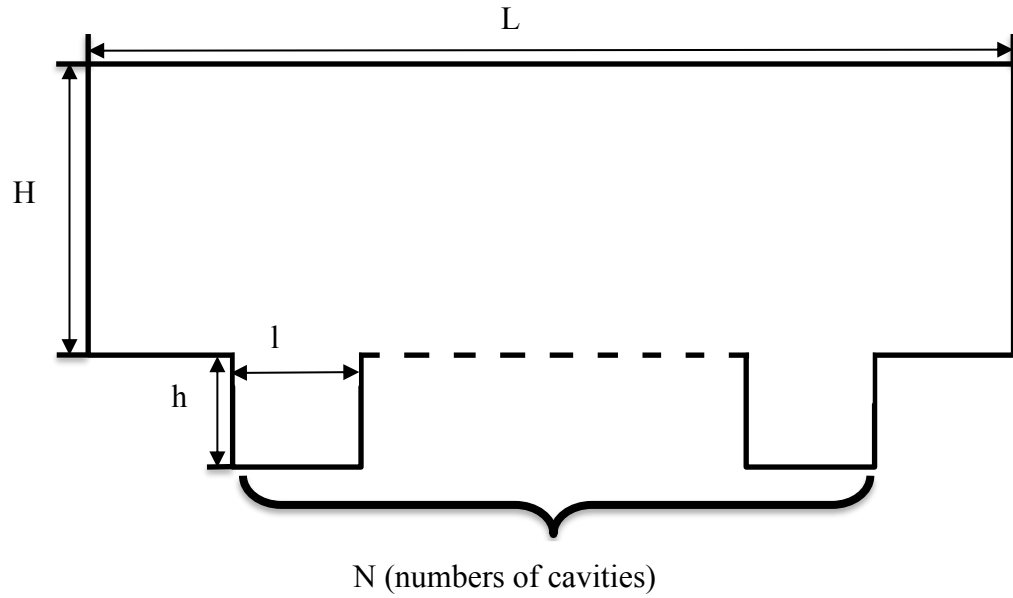
Figure 2.1: Geometry of the model

CASE	H (μm)	L (μm)	l (μm)	h (μm)	N (μm)
1			2	2	1
2			3	2	2
3	6	20	2	2	3
4			6	2	1
5			6	1	1
6			6	0.5	1

Table 2.1: Geometry parameter of the model

2.2.1 Initial and Boundary Conditions

Water is designated as the primary phase and air as the secondary phase. The density of air is assumed to be ideal gas, and will be considered as compressible gas. The fluid properties such as density and viscosity are computed as average properties of individual phases weighted by volume fraction. The Operating Pressure is set as 1 atm. For incompressible flow, the inlet total pressure and the static pressure, p_s are related to the inlet velocity via Bernoulli's equation:

$$p_0 = p_s + \frac{1}{2}\rho v^2 \qquad (2.3)$$

where p_0 refers to the total pressure, p_s is the static pressure and $\frac{1}{2}\rho v^2$ is the dynamic pressure.

The top and bottom surfaces are defined as wall boundaries (no-slip boundary condition). The left-hand vertical edge is defined as the velocity inlet boundary, and the right hand vertical edge is defined as the pressure outlet boundary.

The inlet boundary conditions are either velocity inlet or total pressure inlet in the simulations. In the case of velocity inlet, the total pressure is not fixed but will rise to whatever value is necessary to provide the prescribed velocity distribution. A fully developed flow is compiled using UDF (user defined function). Consider a fluid entering the channel at a uniform velocity. Because of the no-slip condition, the fluid particles in the layer in contact with the fluid particles in the adjacent layers to slow down gradually as a result of friction. Thus, for a fluid flow in the hydrodynamic entrance region of a channel, the wall shear stress is the highest at the inlet where the thickness of the boundary layer is smallest, and decreases gradually to the fully developed value. Therefore, the pressure drop is higher in the entrance region, and the effect of the entrance region is always to increase the average friction factor for the entire channel.

The outlet boundary condition is static (gauge) pressure of 0 pascal. Backflow may occur at pressure outlet boundaries during solution process or as part of solution. Backflow is assumed to be normal to the boundary. Convergence difficulties minimized by realistic values for backflow quantities. Value specified for static pressure used as total pressure where backflow occurs.

Model	Volume of fluid (VOF)
Flow field	2D, Laminar, Incompressible flow
Fluid properties	Water: rho=998.2kg/m^{-3}, viscosity μ=0.001003kg/m·s
	Air: Compressible Ideal Gas
Boundary condition	Velocity/Pressure Inlet: 10≤Re≤50
	At the pressure outlet boundary: Static (Gauge) Pressure = 0
	Reference Pressure = 101,325 Pa (1atm)

Table 2.2: Parameters of Laminar flow analysis using fluent 14.5

2.2.2 Solver Settings

For discretization, the Standard Scheme is used for pressure interpolation, the SIMPLE scheme is used for pressure-velocity coupling, and the second-order upwind differencing scheme is used for the momentum equation. Wall adhesion is enabled so that the contact angle can be prescribed and a constant surface tension value (σ=0.0712 n/m for air-water) is used.

An explicit scheme of the variable time stepping method is used for the transient VOF calculations. Explicit methods calculate the state of a system at a later time from the state of the system at the current time. A variable time stepping ($\triangle$t) criterion is

adopted by fixing the global maximum Courant number. Here, the Courant number is given by

$$CFL = \frac{\Delta t}{\frac{\Delta x}{u_{fluid}}} \qquad (2.4)$$

where Δx is the mesh size and u_{fluid} is the fluid (water) velocity.

The variable time step method is based on the maximum Courant number near the VOF interface. In all cases, the global Courant number is set at 0.2 according to Gaddam et al.[18] while in their simulation, the CFL is set at 0.25.

Thus, the global time-step Δt_{global} is changed by:

$$\Delta t_{global} = CFL_{global} \frac{\Delta x}{u_{fluid}} \qquad (2.5)$$

The residuals are kept at less than 10^{-7} for convergence. For transient, it takes about one week on personal computer to run the case based on the mesh size and geometry.

2.3   Mesh

The computational mesh was prepared using Ansys meshing. Quadrilateral elements were used with the sweeping meshing scheme. In order to accurately quantify the magnitude of the deformation of the meniscus, two types of meshes are used during the study and the minimum mesh size is reduced to $0.1\mu m \times 0.1\mu m$ near the cavity corner in both cases. Mesh (a) is used to compare the air-trapping initial condition with the preset flat interface assumption, as it required higher accuracy to track the fluid in the whole domain in order to capture the air-water interface. Mesh (b) is used for the parametric study with preset flat interface assumption. The full two-dimensional computational domain for the microfluidic channel consist about 40,000 computational cells，which is shown in Figure 2.2
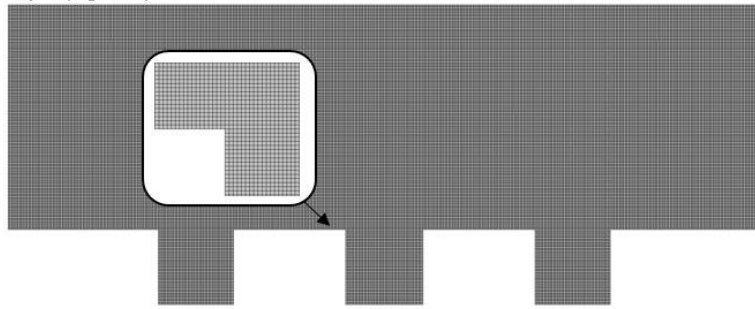
(a)
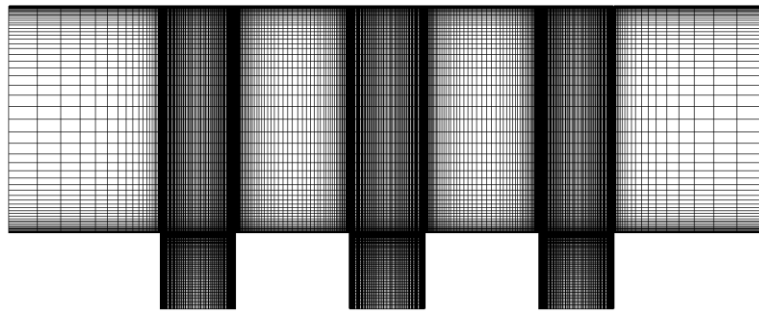
（b）

**Figure 2.2: Mesh of a microchannel with three standard cavities**
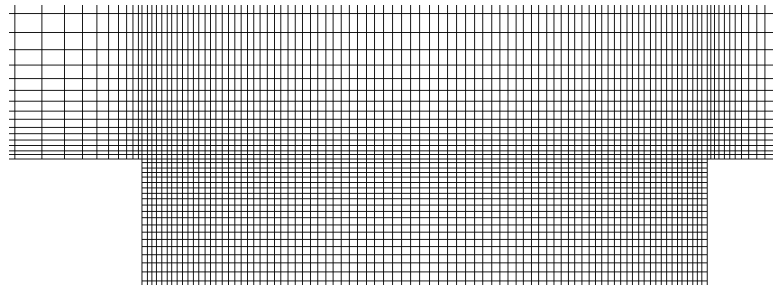
Figure 2.3: Enlarged view of the mesh near the cavity corner for mesh (b)

2.4   Grid Dependency and Validation

2.4.1 Grid Independence Study

The choice of the grid size is a compromise between computational power and required accuracy. More cells will cause more computational time and longer convergence time, but less cells will cause inaccuracy results and will make it difficult to observe the air-water interface due to poor grid solution.

Grid independence was explored by creating coarse, medium and finer meshes in ANSYS meshing (Figure 2.4-2.6). This was achieved by adjusting the bias factor from 5, 25, 2 and 2 to 30, 50, 10 and 6, respectively. The interval sizes of the element on the top and bottom edges was decreased to 0.08, 0.16, 0.04 and 0.03, respectively, for the finer mesh; 0.1, 0.2, 0.05 and 0.04, respectively, for the medium mesh; and 0.3, 0.8, 0.15 and 0.15, respectively, for the coarse mesh. Summaries of the total elements for three types of grids are shown in Tables 2.4, 2.5 and 2.6, respectively.
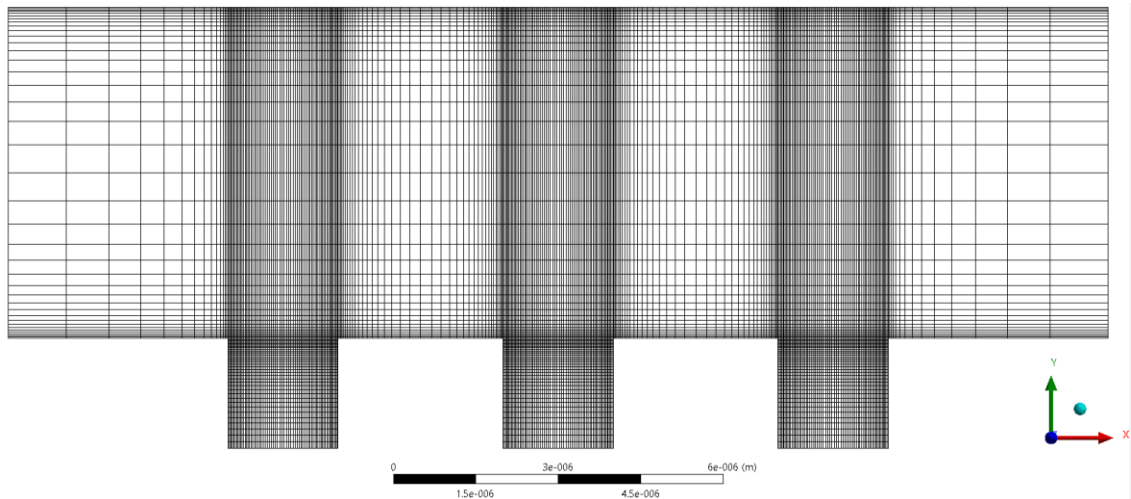
Figure 2.4: Coarse mesh of a microchannel with three cavities.
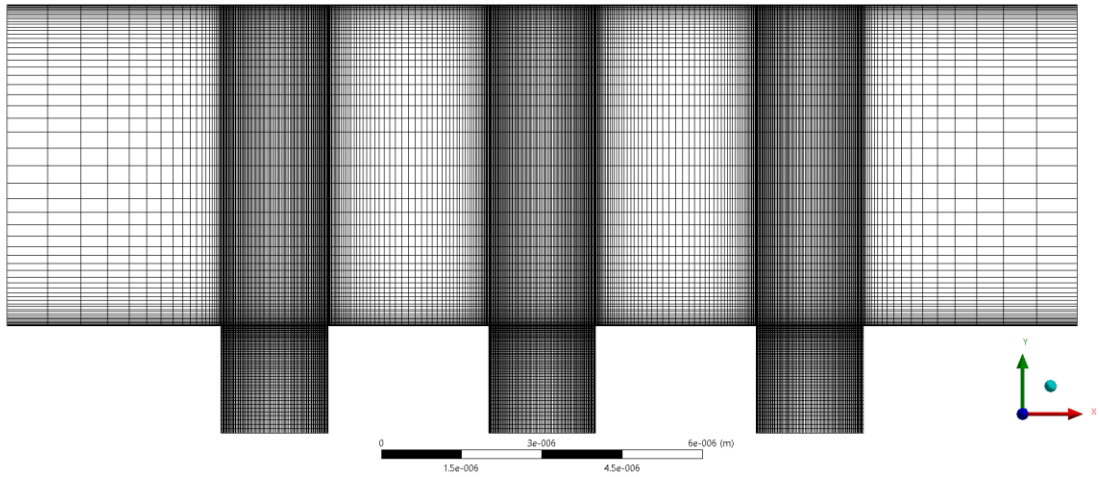
**Figure 2.5: Medium mesh of a microchannel with three cavities.**
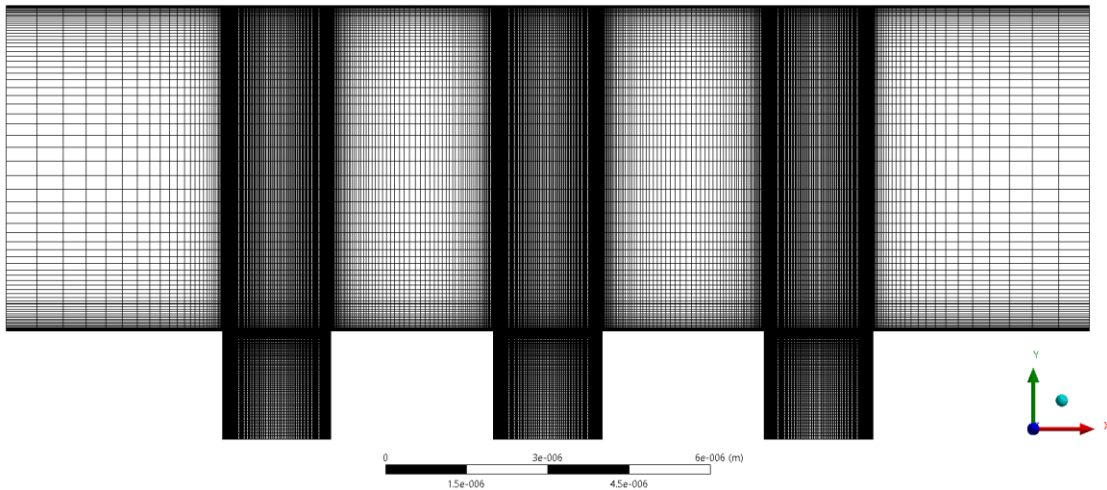
Figure 2.6: Finer mesh of a microchannel with three cavities.

Region	Edge	Bias Factor	Interval Size
Channel	Top Bottom	5	1.6e-7
	Left Right	25	3e-7
Cavity	Top Bottom	2	6e-7
	Left Right	2	6e-7
Total Element	18424		

Table 2.3: Edge Node Assignments for Coarse Mesh

Region	Edge	Ratio	Interval Size
Channel	Top Bottom	25	1e-7
	Left Right	50	2e-7
Cavity	Top Bottom	10	5e-8
	Left Right	6	4e-8
Total element	42600		

Table 2.4: Edge Node Assignments for Medium Mesh

Region	Edge	Ratio	Interval Size
Channel	Top Bottom	30	8e-8
	Left Right	50	1.5e-7
Cavity	Top Bottom	10	3e-8
	Left Right	6	3e-8
Total element	72384		

Table 2.5: Edge Node Assignments for Finer Mesh

To conduct a grid independence test, three simulations are conducted with different grids by changing a global grid sizing parameter.

To get a converge solution for a transient two phase flow problem, the convergence criteria are set as: relative residual of outlet velocity are less than 10-7.

The solution of the coarse mesh is invariant with the finer meshes. The difference between the pressure drop changes less than a tolerance of 5%. Good agreement

between these three meshes is observed. However, for a finer mesh, it takes more than one week to get a converge solution. To get a better resolution of the formation of the air-water meniscus interface and save computational time, the medium mesh is used for further analysis.

2.4.2 Validation with experimental results

The simulation result was validated by comparing the present experimental results with those by Qu et al. [9]. Only bottom sides of the wall have micro-ridges). Simulations have been carried out in the laminar regime of 1<Re<20, which is similar to the work of Qu et al. [9] in order to compare the numerical results.

The comparison of the velocity profile across y-direction through the center of a ridges and the center of the air-water interface are shown in Figure 2.7. In this case, we only simulate one cavity within a microchannel with finite length of L and total pressure is set as inlet boundary condition. Therefore, it can be found that the velocity profile is different at the two centers of ridges, and the velocity profile at downstream ridge appears to have better agreement with experimental data than that at upstream ridge. No evident velocity slip is found at the wall boundary in Figure 2.7 (a). However, the velocity profile near the air-water interface shows a dramatically reduced velocity gradient and therefore a significantly recued shear stress (Figure 2.7 (b)).
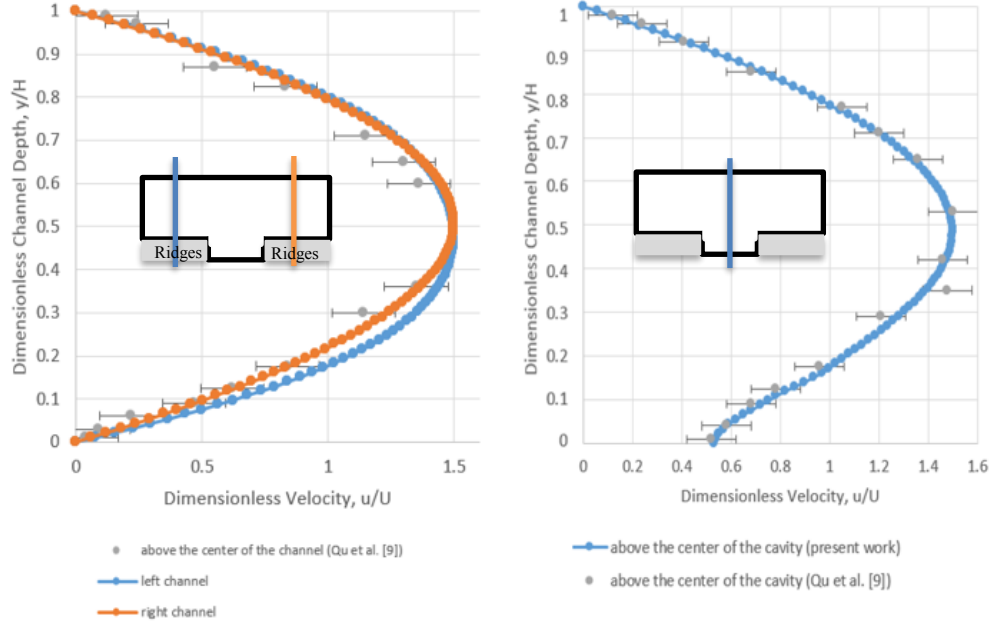
Figure 2.7: Comparison of dimensionless velocity profiles with experiment results at different channel position (a) above the ridge; (b) above the cavity

In these simulations, the classical Darcy friction factor-Reynolds number product, $f \cdot Re$, is calculated. f is the average friction factor in the channel and Re is the Reynolds number ($Re = \rho u_{in} D_h / \mu$).

$$f \cdot Re = \frac{2\Delta P D_h^2}{u_{in} \mu L} \tag{2.6}$$

In the above, ΔP is the total pressure drop across the channel, D_h is the hydraulic diameter ($D_h=2H$), H is the spacing between the top and bottom walls, u_{in} is the inlet velocity to the channel, μ is the dynamic viscosity of water and L is the distance between the inlet and outlet. For a classical Poiseuille flow through a smooth channel, the Poiseuille number is given by $f \cdot Re = 96$. However, in our study, the flow is not fully developed and the velocity profile is quite different due to the entrance effect. Hence, a clean microchannel with pressure inlet has been studied. The standard Poiseuille number in present work is calculated as $f \cdot Re = 90.27$ and will be evaluated in the following sections.

The normalized effective slip length is a function of product of the Darcy friction factor and Reynolds number ($f \cdot Re$) for channel flow and expressed is as (Maynes et al. [9]),

$$\frac{\lambda_T}{H/2} = \frac{32}{f \cdot Re} - \frac{1}{3}$$

(2.7)

This expression is used to compare the present numerical predictions with the experimental results of Qu et al. [5] shown in Figure 2.8.
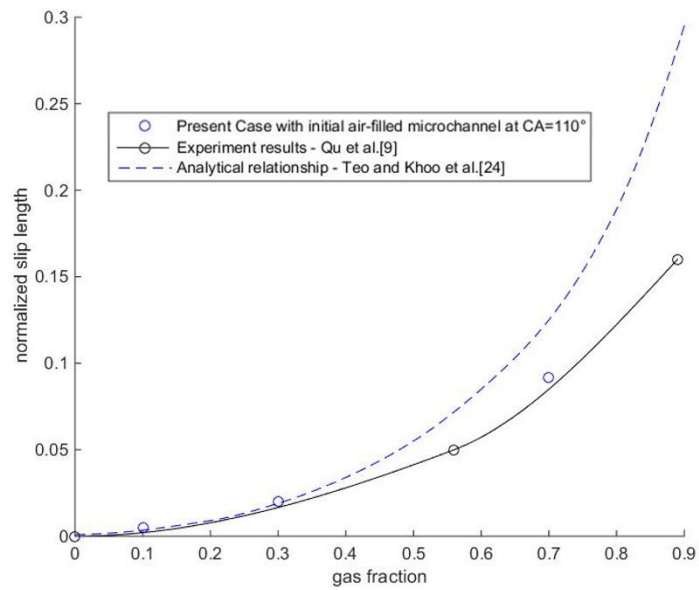

Figure 2.8: Variations of normalized effective slip length with cavity fraction

Chapter 3. Results and Discussions

The effects of wettability and different geometries will be discussed under different initial conditions. In section 4.1, the effects of initial interface assumptions are studied with both preset interface and initially air-filled microchannel. Section 4.2 expands upon the study done in previous section with wettability control. Section 4.3 to 4.5 explores the parametric study of the geometries. Here, the effects of cavity depth, gas fraction and cavity numbers have been investigated.

3.1   Effects of initial boundary condition

3.1.1 Inlet boundary condition

In this section, both velocity and total pressure inlet boundary conditions are simulated in a microchannel with a single cavity.

Velocity inlet boundary conditions are used to define the velocity and scalar properties of the flow at inlet boundaries. In the case of velocity inlet, the total pressure is not fixed but will rise to whatever value is necessary to provide the prescribed velocity distribution. A fully developed flow is compiled using UDF (user defined function). This boundary condition is intended for incompressible flows.

Pressure inlet boundary conditions are used to define the total pressure and other scalar quantities at flow inlets. In the case of total pressure inlet, the mass flow rate is not fixed.

No obvious difference is found between two different inlet boundary conditions. Many numerical simulations used velocity inlet as an initial boundary condition.

compressible flow. Pressure inlet boundary condition is used in further studied because it is more in line with the actual situation.

3.1.2 Initial interface assumption

Most existing numerical simulations have been performed with the assumption that the air-water interface is flat initially [13-17]. With this assumption, the resulting effective slip lengths are different from the experimental results at high gas fraction. Researchers observed that the liquid-gas meniscus curvature might have been the reason for the difference between the numerical solution and experimental results [12]. In the experimental work of Kim et al. [23], they found that the penetration of liquid into the gas cavity have a large effect on the effective slip length. Furthermore, Davis's [24] experiment results indicated that the flow resistance decreases (or the effective slip length increases) when the deformed interface protrudes into the gas cavity.

Since the behavior of the liquid-gas interface has a pronounced effect on the effective slip length and thus on flow resistance, the evolution of liquid-gas interface with two differential initial condition will be investigated judiciously. One is with an initially air-filled microchannel and water flows from the inlet. The other is with a preset flat interface initially at the cavity.

Two parallel cases are studied in the same microchannel with different initial interface conditions. The contact angle (CA) is 90° at the channel wall and 160° at the cavity wall. Figure 3.1(a) shows a channel with initial liquid-air interface at inlet (CASE 1). Water flows from the inlet and expel the air to the outlet. Figure 3.1(b) is the case of preset flat interface (CASE 2). Air patterns are initially trapped inside the cavities and is compressed due to the pressure differences between water and air.

(a)

(b)
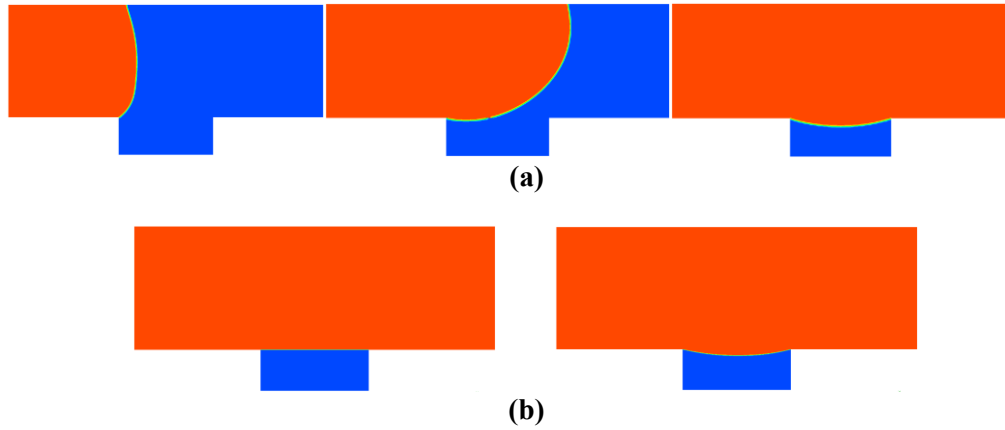
Figure 3.1: Hydrophobic cavity with (a) initially air-filled microchannel, (b) initially preset flat interface

Both two cases formed a meniscus curvature inside the cavity. The final interface shapes obtained with two different initial conditions are shown in Figure 3.2. The orange line is evolved from the initially preset flat interface and the blue line is the result of full air-filled microchannel. It can be found that the interface sinks deeper into the gas cavity in CASE 1. Note that the volume and density of the air in CASE 1 ($mass_{gas} = 1.33{\times}10^{-11}$ kg/m) is smaller than those in CASE 2 ($mass_{gas} = 2.74{\times}10^{-11}$ kg/m), which means air will from the cavities during the liquid transportation.
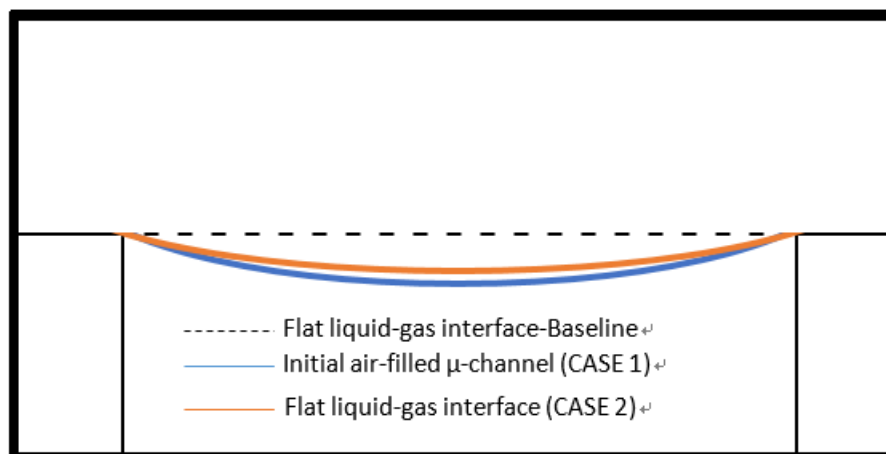

Figure. 3.2: Liquid-gas interface deformation along the length of the cavity

Since the curvature observed is for a single cavity, one should note that the liquid-gas meniscus continuously changes with respect to diminishing static pressure along the length of the channel. The high pressure at the inlet causes more penetration of liquid into the gas cavities (Figure. 3.3) which is consist with the experiment results of Kim et al. [23]. In this case, the gas fraction is remained at 0.3. The contact angle is 90° at the wall of the channel and 160° at the surface of the cavity. Flat interface is set at initial condition.
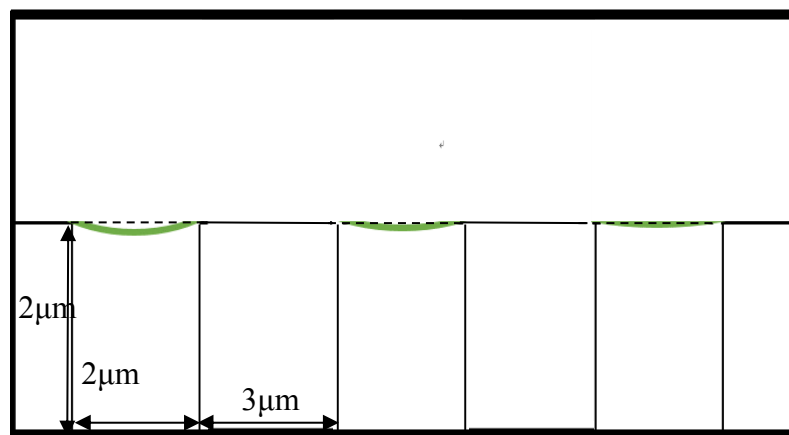

Figure. 3.3: Liquid-gas interface deformation along the length of three cavities

Small deviation between two assumptions are found. A reduction in the friction resistance of 11.68% is observed (f • Re=79.7177) for an initial air-filled microchannel with $F_g = 0.3$ (F_g is the gas fraction, which means the ratio between the area of air-water interface and the solid wall) and CA=160°(contact angle). But for a preset interface, a reduction in friction of 11.90% is predicted (f • Re=79.5209). It can be concluded that the influence of drag reduciton between preset interface and initially air-filled microchannel is negligible at lower gas fraction.

Interface assumptions	Initial air-filled μ -channel Case 1	Preset flat interface Case 2
Inlet velocity (m/s)	4.0318	4.0413
Air mass per length (kg/m)	1.33E-11	2.74E-11
Outlet Dynamic Pressure (Pa)	10861.174	10615.956
Total Pressure Loss (Pa)	22138.826	22384.044
f·Re (clean channel: 90.27)	79.7177	79.5209
Friction Reduction (%)	11.68%	11.90%

**Table 3.1: Comparison between two interface assumptions in microchannel
with a superhydrophobic cavity (CA=160°)**

When we changed the cavity wall from superhydrophobic (160 °) to superhydrophilic (20°), the results between those two assumptions are totally different (Figure 3.4).


(a)

(b)
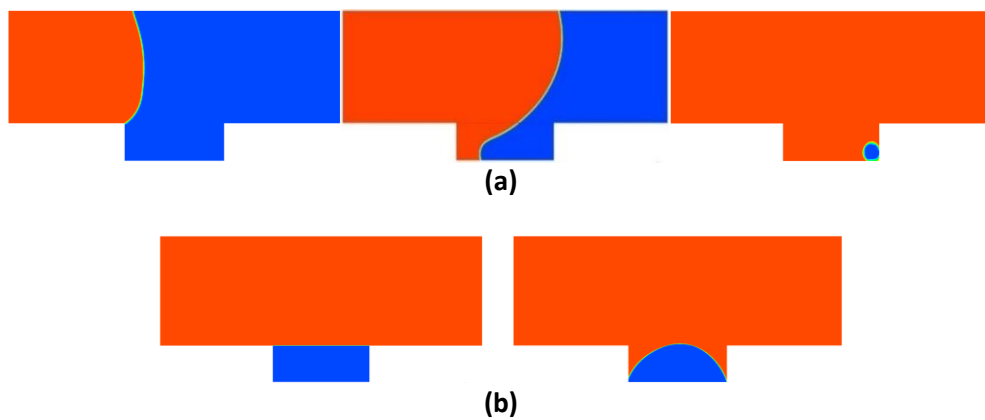
Figure 3.4: Hydrophilic cavity with (a) initially air-filled microchannel, (b) initially preset flat interface

Hydrophilic surfaces have an affinity for water and repel air out of the cavity. For the air-filled microchannel (CASE 3), the air-water interface dispersed and almost wets the whole channel during the transportation. However, for the initially preset interface (CASE 4), the air bubble cannot escape from the cavity. It was compressed by the pressure and formed a different meniscus shape opposite to the hydrophobic case.

Note that flow resistance with superhydrohilic surface increase of 18.26% (f $\cdot$ Re=106.75) for CASE 3 with $F_c = 0.3$ and CA=20° (contact angle). But for CASE 4, a reduction in friction of 13.38% is predicted (f $\cdot$Re=83.42). The details of the number are listed in table 3.2. Studies also found that if decreasing the depth-to-width ratio of the cavity to 0.1, the water flow will completely wet the bottom of the channel as well as the cavity, and the drag performance get worse.

Interface assumptions	Initial air-filled μ-channel	Preset flat interface
Inlet velocity (m/s)	3.47	4.11
Inlet Total Pressure (Pa)	33000	33000
Outlet Dynamic Pressure (Pa)	7207.5	9100.68
Total Pressure Loss (Pa)	25792.5	23899.32
f·Re (clean channel: 90.27)	106.75	83.42
Friction Reduction (%)	-18.26%	13.38%

Table 3.2: Comparison between two interface assumptions in microchannel with a superhydrohilic cavity (CA=20°)

3.2   Effects of surface wettability

In the previous section, the results show that not only the initial interface condition, but also the wettability of the cavity, can have a large effect on slip length and skin-friction reduction. To extend the study on wettability control, different contact angle from 90° to 160° have been simulated.

The contact angle of a drop dispensed onto a solid surface is not unique but can vary over a finite range at sharp corners. Gibb's criterion [25] expresses a continuous variation of the actual angle, at a certain position of the three-phase contact line with in the range of

$$\theta_a \leq \theta^* \leq \theta_a + \varphi$$

where φ represents the geometrical edge angle illustrated in the Figure 3.5 and θ_a is the advancing contact angle. The interface can be pinned at corners within this range of contact angles as long as the pressure balance between inner cavity and outer channel liquid can be achieved.
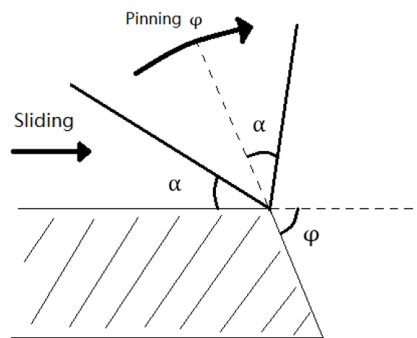
Figure 3.5: Gibb's pinning on a sharp corner

For an initial air-filled microchannel with contact angle of 160^0 and gauge total pressure of 33000Pa, the contact line pinned at cavity corner is shown in Figure 3.6 (a). In this case, the product of surface tension and contact angle θ* is sufficient to establish an interface curvature which can balance pressure difference between outer channel

liquid and inner cavity air. However, when contact angle is reduced to 90°, the surface tension cannot provide any up pulling effect to develop curved interface. Therefore, the interface slides down to reduce the volume of air cavity and to increase the inner cavity air pressure for balancing the outer liquid flow pressure as shown in Figure 3.6 (b).


(a) CA=160° (curve)　　　　　(b)CA=90° (penetration)
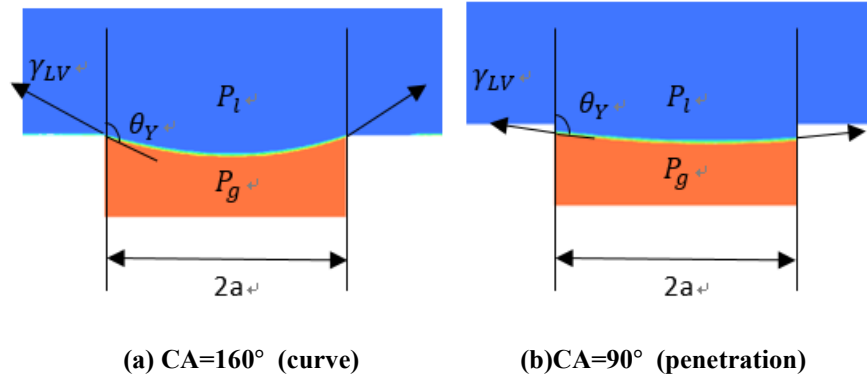
Figure 3.6: Meniscus shape of air-water interface at with (a) CA=160°, (b) 90°

Figure 3.7 shows the pressure contour in the channel with different contact angle (from 90° to 160°) along the whole bottom surfaces and the microchannel is initially filled with air. Thin air layer was found when the surface is superhydrophobic with the contact angle of 160°. Results show that larger pressure difference across high curvature meniscus is found when the contact angle is increased. This can be explained with Young-Laplace equation.

$$\Delta p = \frac{2\sigma\cos\theta}{a} \qquad (2.8)$$

where σ is the surface tension and θ is the contact angle.

Consequently, larger pressure in the cavity occurs at the contact angle of 90°. This is the result of volume reduction by sliding the interface toward the bottom of cavity so that the air pocket is compressed. With this contact angle, there is no curved meniscus to utilize surface tension for up-pulling.

Figure 3.7 also shows that there is an obvious pressure difference around the corner of the cavity. Water begins to accelerate as the wall boundary condition changes from

no slip to slip condition when it flows into the cavity at the left corner, and decrease when it flows out of the cavity at the right corner. According to the Bernoulli's Equation, as the velocity of a fluid increases, the portion of its energy going toward kinetic energy increases, and thus the portion of is energy going toward pressing on the channel decreases.
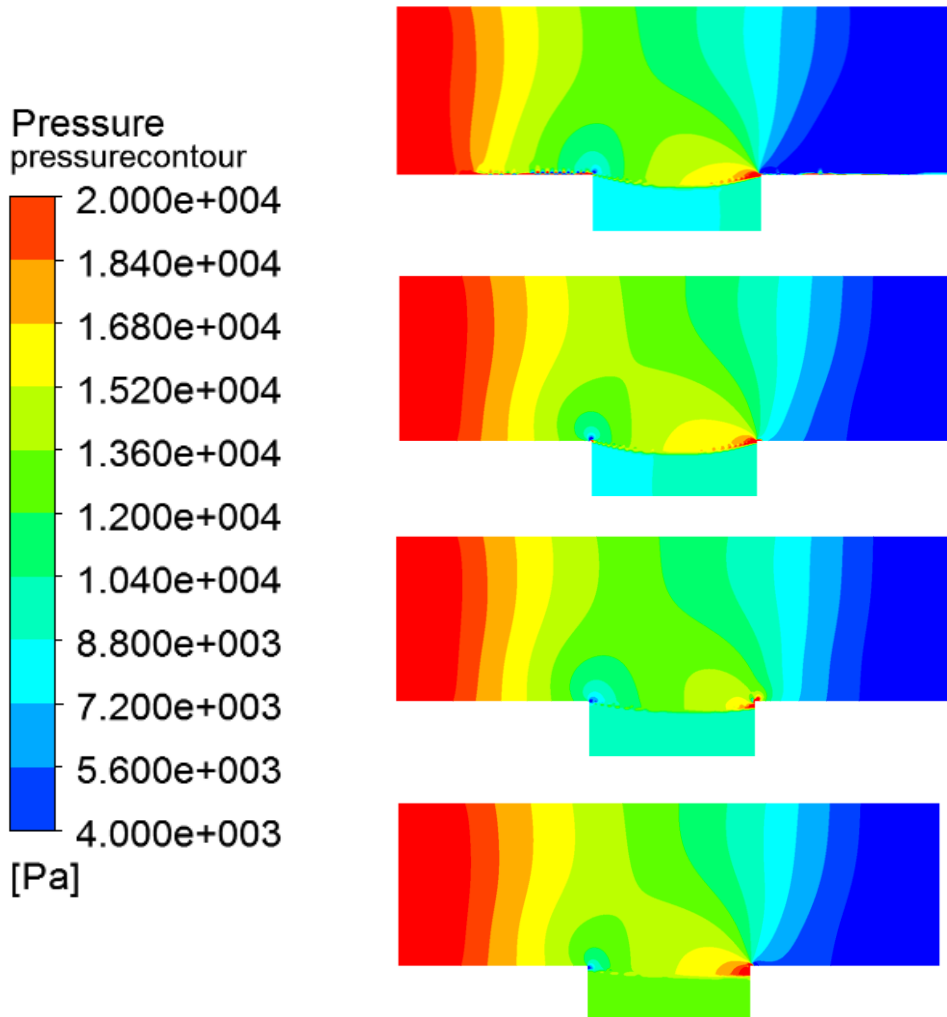

Figure 3.7: Pressure contour with different wettability (a) CA=160, (b) CA=110, (c) CA=100, and (d) CA=90

The streamlines of the fluids near the cavity are shown in Figure 3.8 at different contact angle. Water begins to accelerate when it flows from the wall to the cavity. It is obvious that water protrudes into the cavity with CA=90°. When increasing the contact angle, two vortices generated inside the cavity.

(a)

(b)

(c)
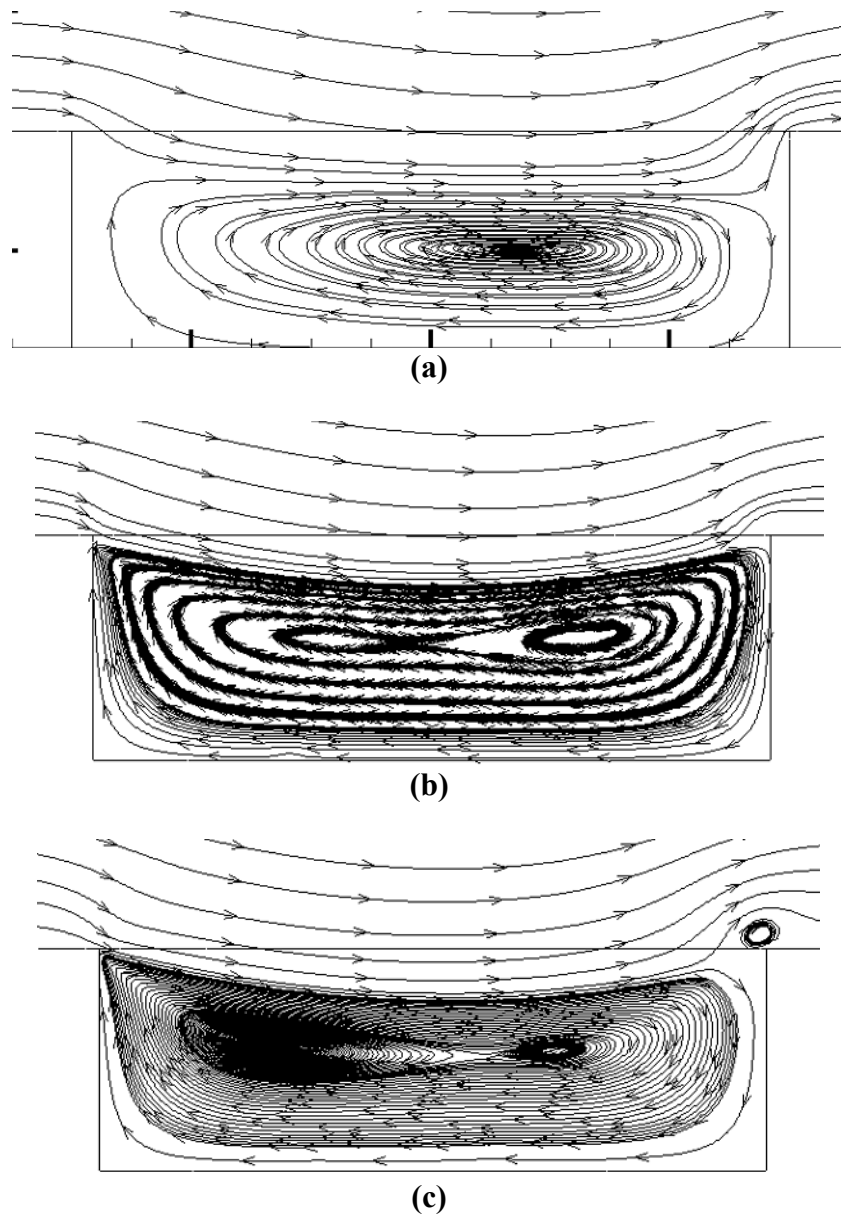
Figure 3.8: Streamline inside the cavity with different contact angle (a) 90^0, (b) 110^0, and (c) 160^0

Fluid moving along solid boundary will incur a shear stress on that boundary. The shear stress at a surface element parallel to a flat pate at the point is given by:

$$\tau = \mu \left(\frac{\partial u}{\partial y} + \frac{\partial v}{\partial x} \right) \tag{2.9}$$

where μ is the dynamic viscosity of the flow, u is the flow velocity along the boundary.

The shear stress at x direction along the microchannel at Plane 1 are shown in Figure 3.9. Hydrophobic surfaces have little tendency to absorb water and the flow is less attracted by the solid surfaces. Therefore, the velocity of the fluid at u direction decreases, resulting in an increasing shear stress near the cavity corner. However, when the fluid flows from the solid wall to a liquid-gas interface, it begins to accelerate due to the change of the wall boundary condition from no-slip to slip. Large velocity gradient jump is found from positive to negative. At the liquid-gas interface, the shear stress becomes smaller because of the lower surface tension. Figure 13 shows that with increasing contact angle, the velocity gradient becomes larger at the corner of the cavity and is smaller at the liquid-gas interface. The osillation of the the shear stress near the corner of the cavity along the air-water interface is due to the vortex shedding.
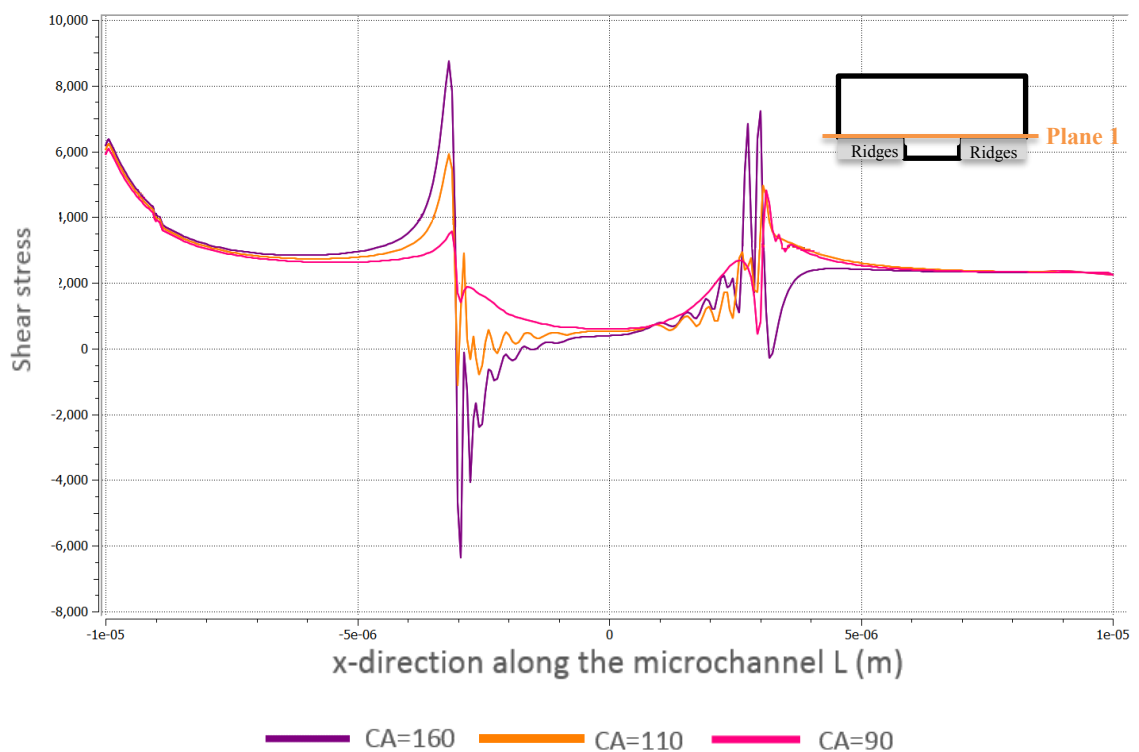

Figure 3.9: Shear stress at Plane 1 with different contact angle

The interface remains pinned to the corner of the cavity and the shape of the interface becomes more curved with larger contact angle. It is observed that slip length as well as the friction reduction will increase with the increasing hydrophobicity (Figure.

3.10). On the other hand, the interface begins to slide down at contact angles less than 1100 and penetrate the cavity at smaller contact angle. As a result, the liquid-solid contact surface is increased at the vertical surfaces of cavity. Our research also shows that if the meniscus protrudes more into the void surface structures, the slip length will decrease, which is consistent with the theoretical studies [25,26,27].
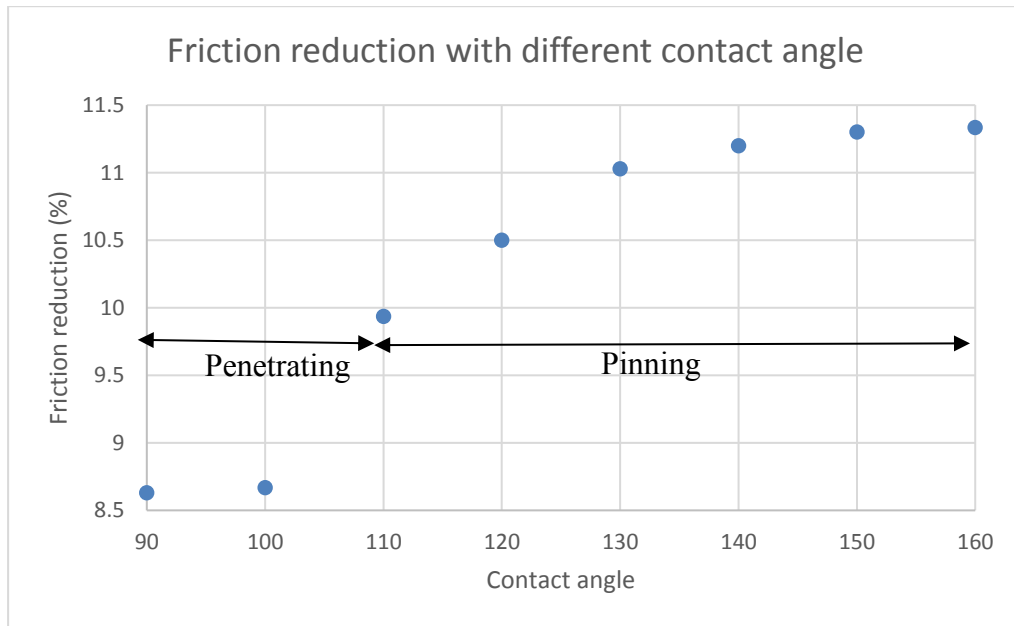

Figure 3.10: Friction reduction with different contact angle

Contact angle	90°	100°	110°	160°
Inlet velocity (m/s)	3.94	3.96	3.99	4.05
Inlet Total Pressure (Pa)	33000	33000	33000	33000
Total Pressure Loss (Pa)	22622.36	22750.2	22595.6	22595.6
f·Re (clean channel: 90.27)	82.48	82.44	81.3	80.04
Friction Reduction (%)	8.63%	8.67%	9.93%	11.33%

Table 3.3: Comparison between cavities with different contact angle

3.3 Effects of cavity depth

Researches have been found that the depth-to-width ratio of the cavities between adjacent micro-ridges is an important effective parameter for the flow in the micro-channel. For the larger depth-to-width ratio, it is easy to keep the air in the cavities. (Li et al, 2015).

In this section, the effects of cavities depth have been studied. The geometry and parameters are listed in Figure 3.10. The width of the cavities is fixed as 6μm. The depth of the bigger cavity is changed from 2μm to 1μm, 0.5μm. Thus, the depth-to-width ratio from 0.083 to 0.333 is studied under the same pressure driven flow. The reduction fRe is listed in the following Table.
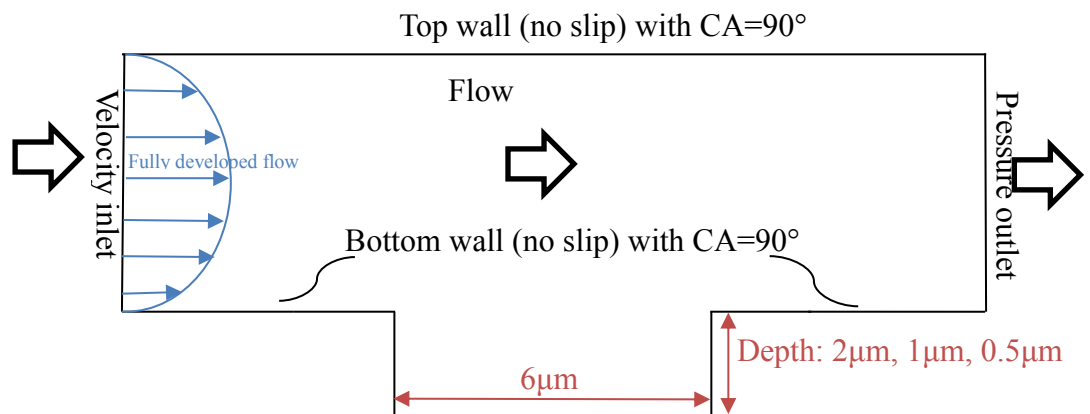

Figure 3.11: Scheme of channel with different depth

Depth	Reynolds number (outlet)	Reduction of fRe
2μm	44.16	9.8%
1μm	44.19	9.8%
0.5μm	44.04	9.3%

Table 3.4: Friction reduction by air-trapping in the cavities with different depths

It can be found that the depth has insignificant effects on the reduction of friction. This can be explained by the similar velocity profile in the water field show in Figure. The velocity at the air-water interface is almost the same at different depth of channel. Thus, the difference of the shear rate at the interface is small, resulting in small deviation of drag reduction.
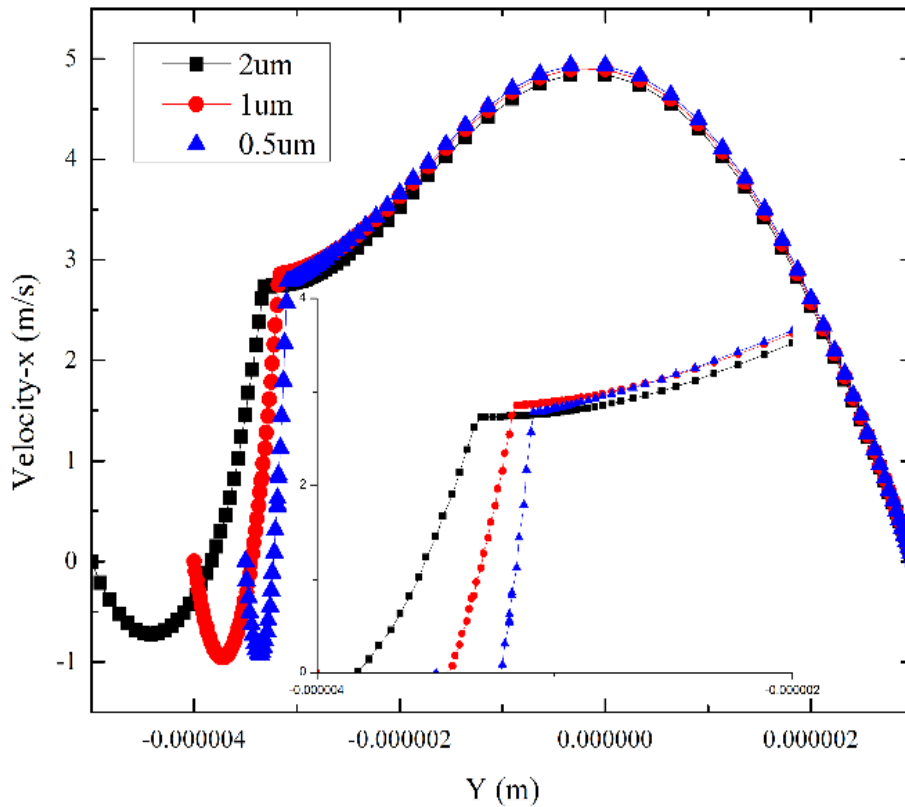

Figure 3.12: Velocity Profile of different channel depth

Gaddam et al. [18] found that the amount of overhang of the meniscus increases with the gas fraction.It also can be found that with the same gas fraction,

Figure 3.12 shows the deformation profile for gas fraction varied from 0.2, 0.4, 0.6 and 0.7. Here, the magnitude of the deformation (Δ) is normalized with the height of the cavity (H), while the x-coordinate is normalized by the length of the cavity (Ls).
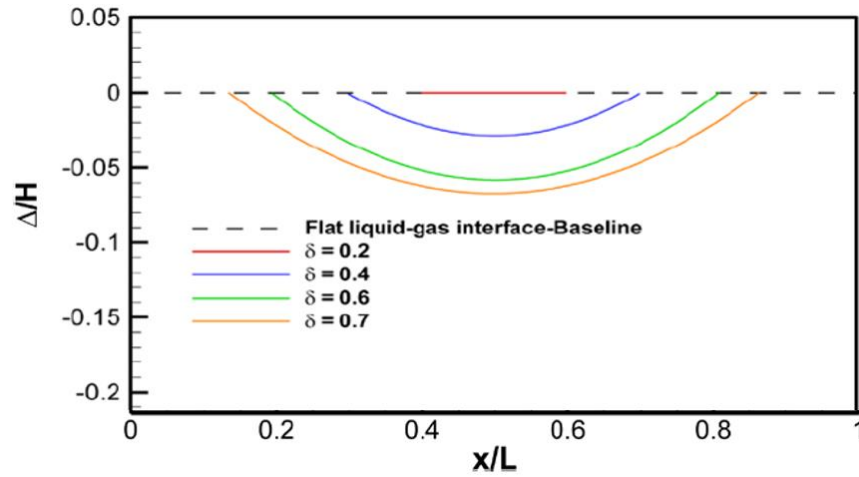
Figure 3.13: Shapes of air-water interface with different gas fraction

It is observed that the amount of overhang of the meniscus increases with gas fraction. As can be observed, the amount of the deformation increased with the gas fraction.

In our research, it is found that the depth also has small effects on the deformation of the air-water meniscus interface. As the depth-to-width ratio decrease, the interface becomes more flat.
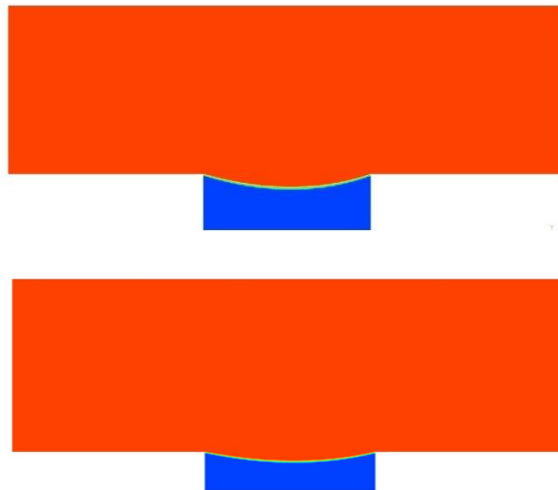

Figure 3.14: Air-water interface with different cavity depth at the same gas fraction

3.4   Effects of gas fraction

In earlier numerical works of Maynes et al. [13] and Davies et al. [16], only a single rib-cavity module was considered for evaluating the effective slip length. It was reported that the effective slip length decreases with gas fraction. Research has also shown that the smaller the solid area fraction, the greater the slipping velocity on the air-water interface [33].

Based on their research, different cavity coverage are studied ranging from 10% to 70% (According to Qu's paper [9], the cavity coverage was optimized from 16.67% to 66.67%). Results show that larger gas fraction has better performance on drag reduction, and the drag friction increase with cavities numbers.
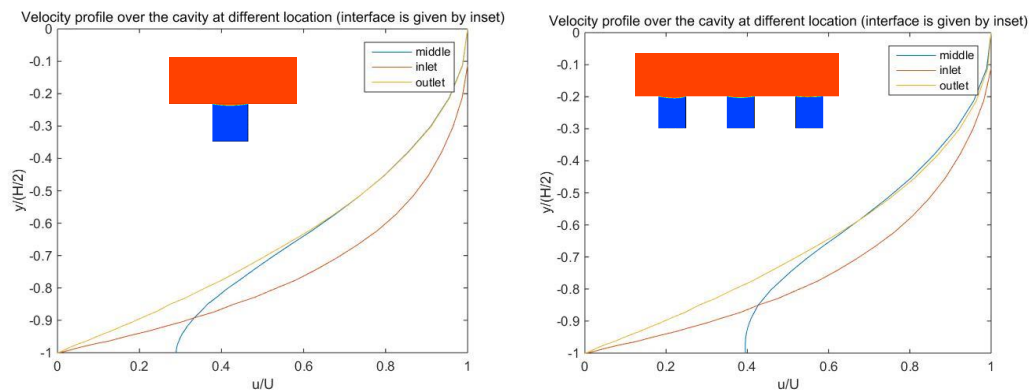

Figure 3.15: Velocity profile over the cavity at different location

As shown in figure, the numerical simulations are performed on a 2D surface element. The gas fraction remains constant. The corresponding velocity profiles over the gas cavity are plotted in Figure 10. Here, the normal coordinate is normalized by half channel spacing (H/2) and the velocity is normalized by the maximum velocity U. The velocity profiles are shown in three different locations of the cavity: the inlet of the channel (x=-10e-6m), the middle of the channel (x=0m) and the outlet of the channel (x=10e-6m). It can be observed that the slip velocity is relatively small near the edge of inlet and outlet area and reach to 0 at the wall due to the no-slip boundary

condition. As the flow progresses from the ridge to the cavity, the no slip condition breaks down and the flow starts accelerating near the meniscus reaching a maximum value at the cavity center and decelerating toward the cavity exit.
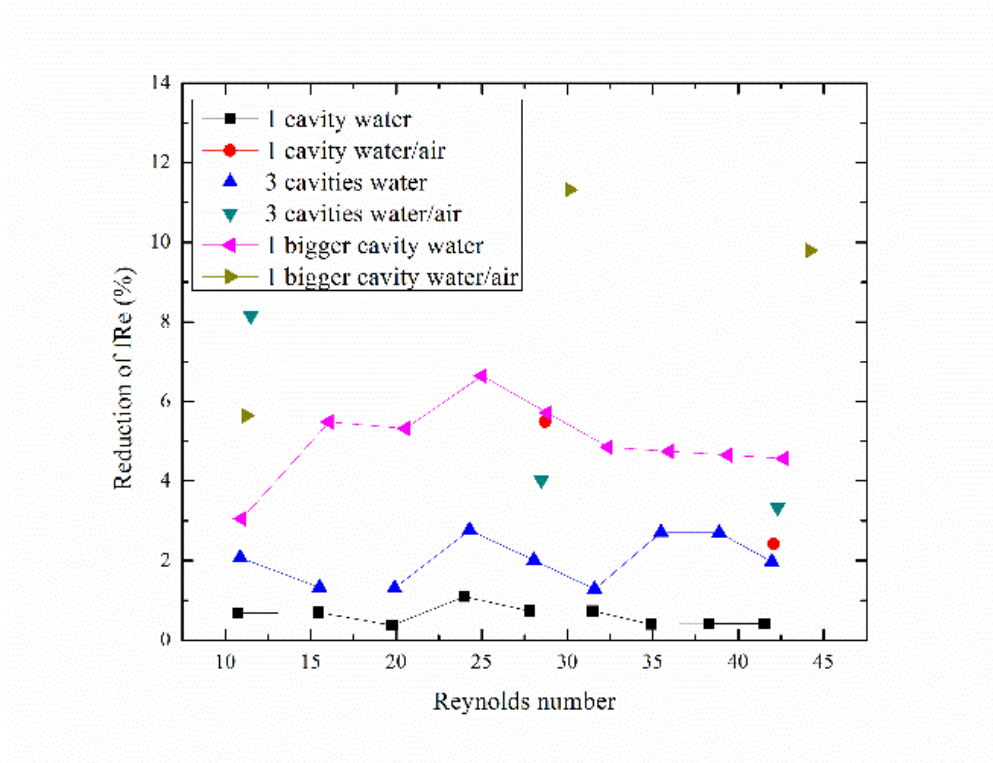

Figure 3.16: Reynolds number vs. Reduction

Figure 9 shows that three standard cavities perform better than one standard cavity as they provide a longer "slip-boundary" condition. At higher Reynolds number, one bigger cavity outperforms other configurations. The maximum reduction of the friction reduction can reach ~19%. This can be explained by the longer and continuous "slip-boundary" condition.

The results also show that three standard cavities perform better than one standard cavity as they provide a longer "slip-boundary" condition. At higher Reynolds number, one bigger cavity outperforms other configurations. The maximum reduction of the friction reduction can reach ~11%. This can be explained by the longer and continuous "slip-boundary" condition. Velocity profiles at the middle of

the micro-channels are compared in Figure 9 while the Reynolds number is 44. It is

reasonable to see the better "slip-boundary" given by the bigger cavity.
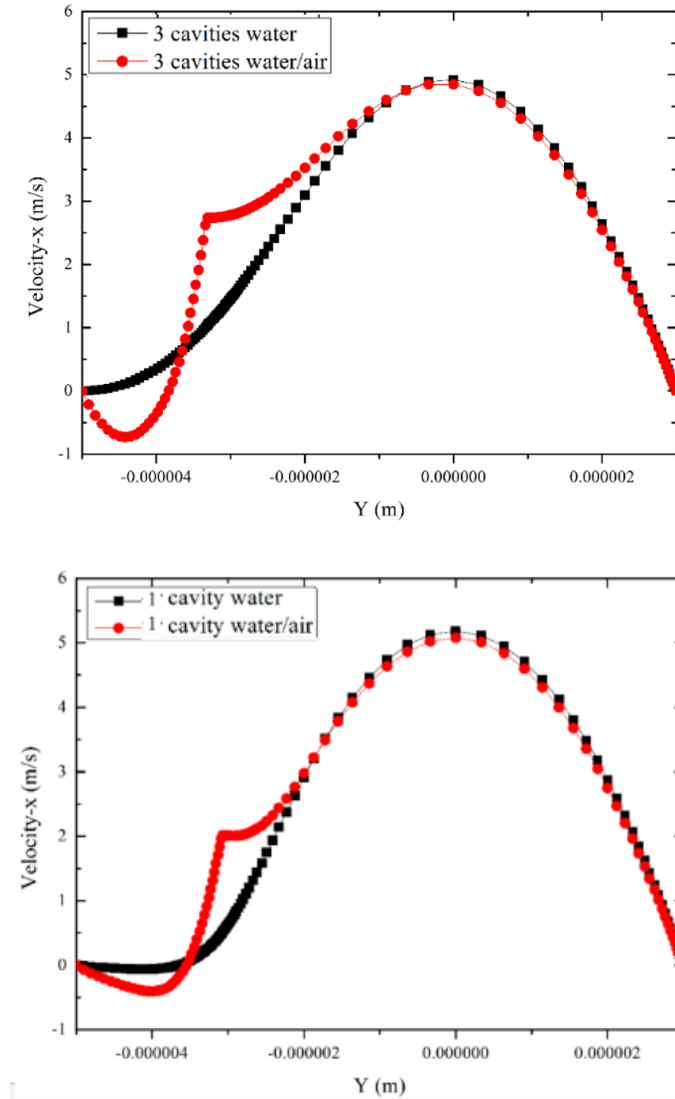

Figure 3.17: Velocity profile along the middle of the channel with different gas fraction

3.5   Effects of cavity number

Based on the earlier section, microchannel with higher gas fraction perform better on drag reduction. This is because the air pocket in the cavities can provide a slip velocity in a shear-free air-water interface. The larger the gas fraction, the more interface it can provide.

In this section, the effects of cavity number is studied by keeping the gas fraction constant. The number of cavities on the bottom wall varied at three levels, i.e. 1, 2 and 3, as showed in the figure.
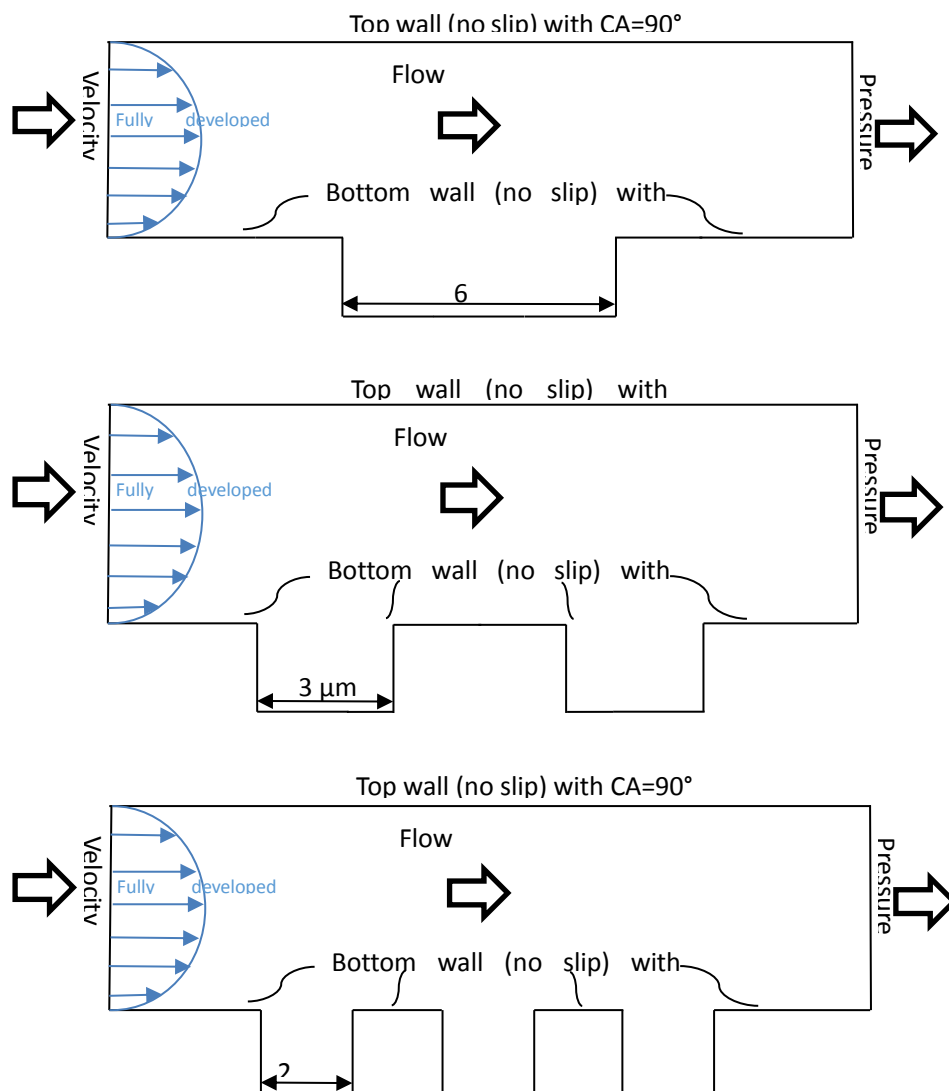

Figure 3.18: Different cavity numbers in microchannel with same gas fraction

As the number of the cavities increases, the fluid experiences more acceleration and deceleration cycles at the air cavity and solid walls, respectively, causing the friction factor to increase. Figure3.16 (a), (b) and (c) show the streamlines along the microchannel with same pressure inlet and gas friction. It can be found that when the fluid pass through a cavity, a vortex generated inside the cavity and the air patterns moving against the liquid phase.
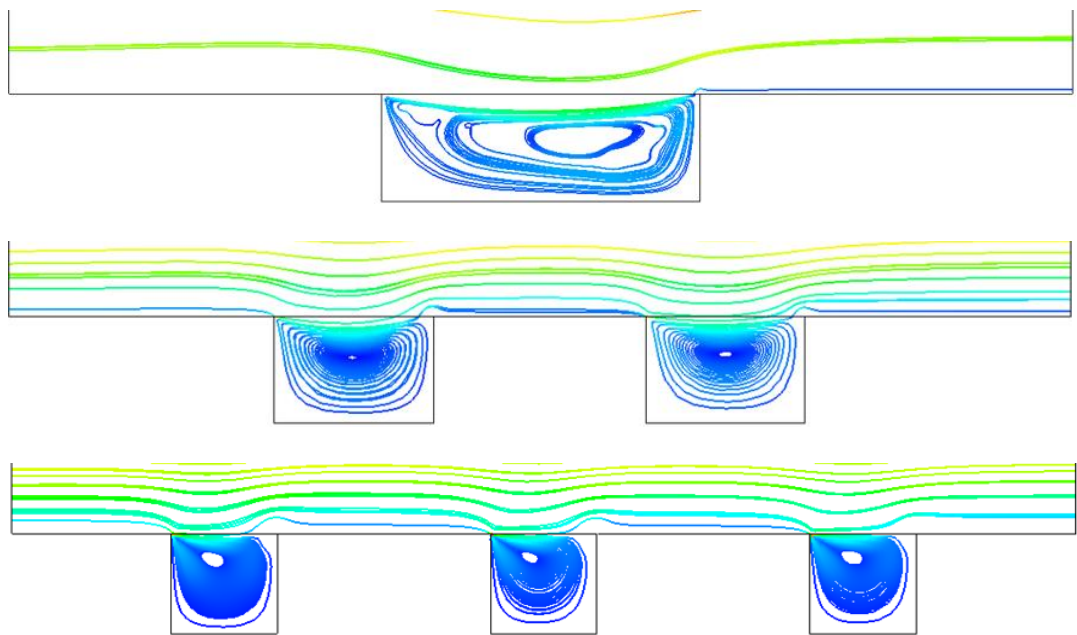
Figure 3.19: Streamline along the microchannel with different cavity numbers

The inset in the figure 3.10 below show that the deformation of the meniscus of one big cavity is also larger than three small cavities. Thus, the amount of overhang of the meniscus is not only increased with gas fraction, but also related to the wide-to-length ratio of the cavity.

The maximum reduction of the friction reduction can reach ~11%. This can be explained by the longer and continuous "slip-boundary" condition. It is reasonable to see the better "slip-boundary" given by the bigger cavity.
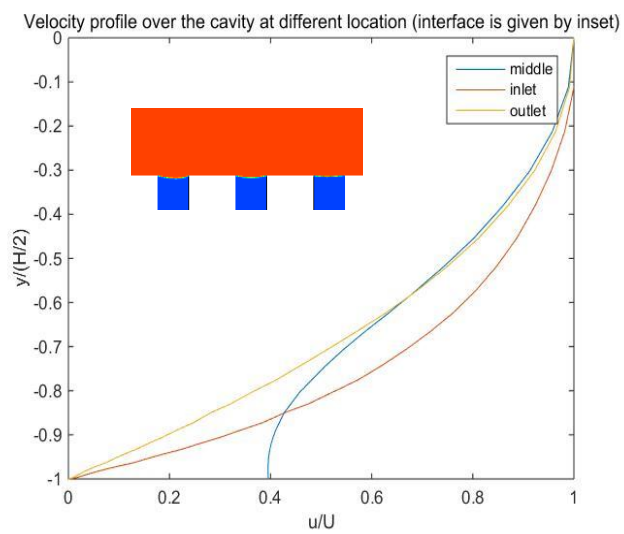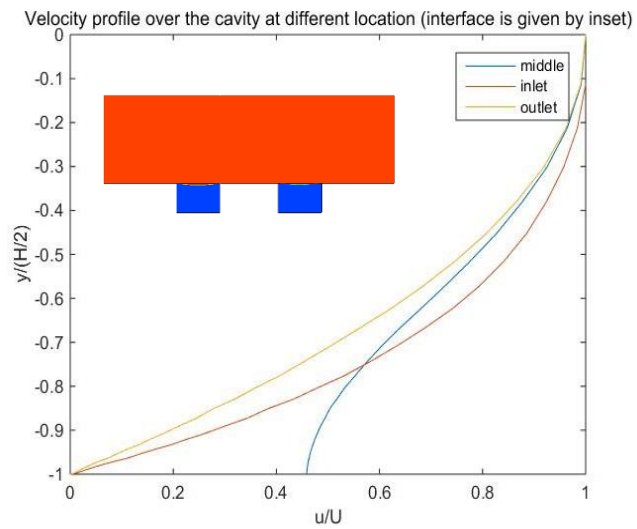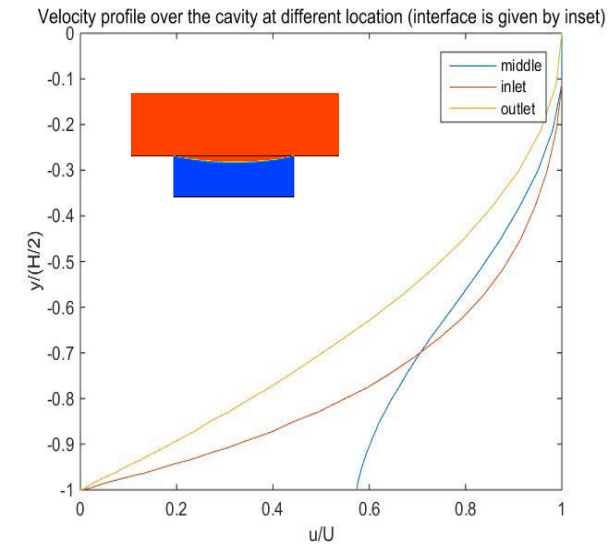
**Figure 3.20: Dimensionless velocity profile with different cavity numbers**
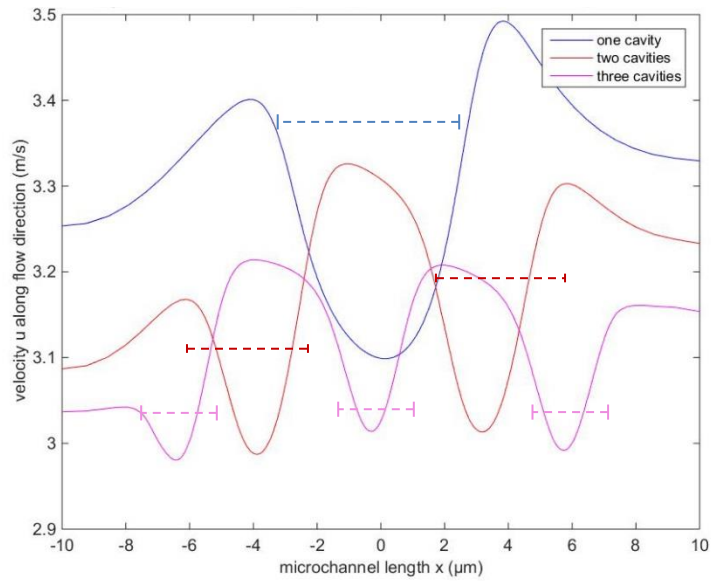
Figure 3.21: Velocity-u profile at 0.1 μ m above the micro-ridges

Figure 3.18 shows that velocity increased when it began to pass through a cavity and decreased in the middle of the cavity. When the flow pass through more cavities, it will experience more acceleration and deceleration. During the acceleration period over the gas cavity, parts of the momentum is transferred into the cavity through viscous diffusion.

As the number of the cavities increases, the fluid experiences more acceleration and deceleration cycles at the air cavity and solid walls, respectively, causing the friction factor to increase.

Chapter 4.   CONCLUSION AND FUTURE WORK

4.1   Summary

Numerical parametrical studies on drag reduction through wettability control in microstructured channel were presented using ANSYS FLUENT 14.5. The parametric studies were performed for incompressible, laminar flows over flat plate of micro-structured channel. Results are summarized as follows:

(1) Four parallel cases are studied with initially preset flat interface (CASE 1, CASE 3) and initially air-filled microchannel assumption (CASE 2, CASE4) at contact angle of 20° and 160°. For the CASE 2 of microchannel with superhydrophobic cavity, water will expel a small amount of air out of the channel during the process and the air-water interface protrudes a little more into the cavity than case one. However, the difference of friction reduction between these two cases is negligible. On the other hand, a large discrepancy is found between CASE 3 and CASE 4 when the cavity is superhydrohilic. In CASE 3, the liquid flow almost completely wets the entire surface and expel the air out of the channel. Flow resistance increases in CASE 3 but decreases in CASE 4.

(2) Skin friction reduction increases with increasing surface contact angle due to different interface shape and liquid-solid contact areas. The deformation of the air-water interface consists of two modes: a) sliding down and b) meniscus modes. Sliding-down mode transitions into meniscus mode when contact angle increases. The pressure changes along the channel during the water transportation. When the contact angle is smaller, the surface tension cannot

provide enough pulling force to develop a curved interface. Therefore, the interface slides down to reduce volume of air cavity and to increase the inner cavity air pressure for balancing the outer liquid flow pressure, resulting in an increasing solid-liquid area. When the contact angle is larger, the contact line of liquid and gas remains pinned and the pressure balance is accomplished by changing the curvature of the meniscus. As a result, solid-liquid area remains the same and total pressure loss is reduced significantly.

(3) Cavity Depth has insignificant effects on the reduction of friction.

(4) Increasing the numbers of cavities provides better performance on drag reduction as they provide more "slip-boundary" condition.

(5) With the same gas fraction, increasing the density of the cavities provides better performance on drag reduction as they provide longer and continuous "slip-boundary" condition.

4.2　Recommendations for Future Work

More cases will be carried out to build the relationship between friction reduction and different configurations in transient state to find a smaller range of depth-to-width ratio in which the cavity can successfully captured the air pockets. Different shapes of posts can be studied to observe the position of the air-water interface because the mechanism for depinning is strongly dependent on the details of the post geometry and on the Young's contact angle, and depinning from both the top and the side edges of the posts is important in controlling the fluid behavior. The effect of air diffusion and how to overcome this effect will be taken into consideration.

Reference

[1] Ho, C.-M. and Y.-C. Tai (1998). "MICRO-ELECTRO-MECHANICAL-SYSTEMS (MEMS) AND FLUID FLOWS." Annual Review of Fluid Mechanics 30(1): 579-612.

[2] Sanders, W. C., et al. (2006). "Bubble friction drag reduction in a high-Reynolds-number flat-plate turbulent boundary layer." Journal of Fluid Mechanics 552: 353-380.

[3] Kim, J. and T. R. Bewley (2006). "A Linear Systems Approach to Flow Control." Annual Review of Fluid Mechanics 39(1): 383-417.

[4] Han, M., et al. (2003). Fabrication of a micro-riblet film and drag reduction effects on curved objects. TRANSDUCERS, Solid-State Sensors, Actuators and Microsystems, 12th International Conference on, 2003.

[5] Cheng Hai, H., et al. (2015). "Turbulent Drag Reduction with Polymers in Rotating Disk Flow." Polymers (20734360) 7(7): 1279-1298.

[6] Philip, J. R. (1972). "Flows satisfying mixed no-slip and no-shear conditions." Zeitschrift für angewandte Mathematik und Physik ZAMP 23(3): 353-372.

[7] Lauga, E. and H. A. Stone (2003). "Effective slip in pressure-driven Stokes flow." Journal of Fluid Mechanics(489): 55-77.

[8] Ou, J. and J. P. Rothstein (2005). "Direct velocity measurements of the flow past drag-reducing ultrahydrophobic surfaces." Physics of Fluids (1994-present) 17(10): 103606.

[9] Ou, J., et al. (2004). "Laminar drag reduction in microchannels using ultrahydrophobic surfaces." Physics of Fluids 16(12): 4635-4643.

[10] Choi, C.-H., et al. (2006). "Effective slip and friction reduction in nanograted superhydrophobic microchannels." Physics of Fluids (1994-present) 18(8): 087105.

[11] C. Lee, C.-H., et al. (2008). "Structured surfaces for a giant liquid slip," Phys. Rev. Lett., vol. 101, p. 064501.

[12] Tsai, P., et al. (2009). "Quantifying effective slip length over micropatterned hydrophobic surfaces." Physics of Fluids (1994-present) 21(11): 112002.

[13] Maynes, D., et al. (2007). "Laminar flow in a microchannel with hydrophobic surface patterned microribs oriented parallel to the flow direction." Physics of Fluids 19(9): 093603.

[14] Cheng, Y. P., et al. (2009). "Microchannel flows with superhydrophobic surfaces: Effects of Reynolds number and pattern width to channel height ratio." Physics of Fluids 21(12): 122004.

[15] Ng CO, Wang., et al. (2009). "Stokes shear flow over a grating: implications for superhydrophobic slip." Physics of Fluids 21:013602

[16] Davies, J., et al. (2006). "Laminar flow in a microchannel with superhydrophobic walls exhibiting transverse ribs." Physics of Fluids 18(8): 087110.

[17] Park, H. (2015). A Numerical Study of the Effects of Superhydrophobic Surfaces on Skin-Friction Drag Reduction in Wall-Bounded Shear Flows.

[18] Gaddam, A., et al. (2015). "Modeling of liquid-gas meniscus for textured surfaces: Effects of curvature and local slip length." Journal of Micromechanics and Microengineering 25(12).

[19] Belaud, V., et al.(2015). "Wettability versus roughness: Multi-scales approach." Tribology International, Part B: p. 343-349.

[20] Cassie, A. B. D. and S. Baxter (1944). "Wettability of porous surfaces." Transactions of the Faraday Society 40(0): 546-551.

[21] Cassie, A. B. D. and S. Baxter (1944). "Wettability of porous surfaces." Transactions of the Faraday Society 40(0): 546-551.

[22] *Young, T. (1805). "An Essay on the Cohesion of Fluids".* Phil. Trans. R. Soc. Lond. *95: 65–87.* doi*:*10.1098/rstl.1805.0005.

[23] Kim, T. J. and C. Hidrovo (2012). "Pressure and partial wetting effects on superhydrophobic friction reduction in microchannel flow." Physics of Fluids 24(11): 112003.

[24] Davies, J., et al. (2006). "Laminar flow in a microchannel with superhydrophobic walls exhibiting transverse ribs." Physics of Fluids 18(8): 087110.

[25] Dyson, D. C. (1988). "Contact line stability at edges: Comments on Gibbs's inequalities." Physics of Fluids 31(2): 229-232.

[26] Biben, T. and L. Joly (2008). "Wetting on Nanorough Surfaces." Physical review letters 100(18): 186103.

[27] Wang, B., et al. (2014). "Investigation of retention of gases in transverse hydrophobic microgrooved surfaces for drag reduction." Ocean Engineering 79: 58-66.

[28] Lee, C., et al. (2016). "Superhydrophobic drag reduction in laminar flows: a critical review." Experiments in Fluids 57(12): 176.

[29] Dyson, D. C. (1988). "Contact line stability at edges: Comments on Gibbs's inequalities." Physics of Fluids 31(2): 229-232.

[30] Teo, C.J., et al. (2014). "Effects of interface deformation on flow through microtubes containing superhydrophobic surfaces with longitudinal ribs and grooves." Microfluidics and Nanofluidics 16(1): 225-236.

[31] Belaud, V., et al.(2015). "Wettability versus roughness: Multi-scales approach." Tribology International, Part B: p. 343-349.

[32] Li, B., et al. (2015). "Incompressible LBGK simulation of flow characteristics in a micro-channel with patterned superhydrophobic surfaces." Applied Mathematical Modelling 39(1): 300-308.

[33] Fluent Manual. Ansys Inc, . [xv, 13, 15, 16, 18, 19, 21, 22, 29, 37, 51, 91, 93, 101, 102]

[34] Zhang, H., et al. (2016). "Wettability and drag reduction of a superhydrophobic aluminum surface." RSC Advances 6(17): 14034-14041.

[35] Park, H. (2015). A Numerical Study of the Effects of Superhydrophobic Surfaces on Skin-Friction Drag Reduction in Wall-Bounded Shear Flows.

[36] Guangyi, S., et al. (2015). "Development of a Miniature Shear Sensor for Direct Comparison of Skin-Friction Drags." Microelectromechanical Systems, Journal of 24(5): 1426-1435.

[37] Guan, N., et al. (2015). "Experimental and theoretical investigations on the flow resistance reduction and slip flow in super-hydrophobic micro tubes." Experimental Thermal and Fluid Science 69: 45-57.

[38] Dilip, D., et al. (2015). "Effect of absolute pressure on flow through a textured hydrophobic microchannel." Microfluidics and Nanofluidics 19(6): 1409-1427.

[39] Chai, L., et al. (2015). "Two-phase flow pattern and pressure drop in silicon multi-microchannel with expansion–constriction cross-section." Experimental Thermal and Fluid Science 60: 241-251.

[40] Brassard, J.-D., et al. (2015). "Studies of drag on the nanocomposite superhydrophobic surfaces." Applied Surface Science 324: 525-531.